AUT Journal of Mechanical Engineering

AUT J. Mech. Eng., 10(3) (2026) 269-296
DOI: 10.22060/ajme.2025.24784.6229

The Novel Analytical Model of Low-Temperature Hydrogen/Oxygen Reactor on Platinum Catalytic Surface in Different Micro-Porous Mediums

Saeedeh Sisban, Seyed Abouzar Fanaee*

Department of Mechanical Engineering, Faculty of Engineering, University of Birjand, Birjand, Iran.

ABSTRACT: This paper presents a comprehensive parametric analysis concentrated to the design of a novel low temperature hydrogen porous micro-reactor. The main important of this work is optimizing the water production process by a complete parametric description. In the analytical solution of this problem, the velocity profile is first determined by solving the momentum equation, and this result is then used in the energy and mass concentration equations to obtain thermal and mass parameters. The solution is achieved through a non-asymptotic solution that concurrently incorporates both mathematical and physical aspects, taking into account the surface reaction rate and matching conditions at the interfaces between the fluid, porous solid, and solid wall boundaries. The maximum variation of Nusselt number in the width of microchannel is observed for the alumina porous medium, with values of 58.70% and 67.69% respectively with 95% and 90% porosities. The rate of hydrogen to water conversion in alumina media is approximately 41% faster than titanium oxide and 67% faster than silicon carbide. The maximum variation of Sherwood number in the width of microchannel is observed for the silicon carbide porous medium, with values of 58.33% and 50.13% respectively with 95% and 90% porosities. As the porosity coefficients increase from 85% to 95% the variation rates of fluid and solid phase temperature is decreased from 78.01% to 45.09% and 65.92% to 35.09%. the porosity coefficient, the rate of hydrogen to water conversion is increased from 43.01 to 75.05%.

Review History:

Received: Sep. 21, 2025
Revised: Oct. 28, 2025
Accepted: Nov. 16, 2025
Available Online: Nov. 23, 2025

Keywords:

Novel Analytical Model
Porous Medium
Catalytic Surface
Hydrogen Reactor

1- Introduction

The reaction of hydrogen and oxygen on a platinum (*Pt*) catalyst is a process that is important for a wide range of industries such as fuel cell manufacturing and chemical processing. In microchannel reactors, the high surface area to volume ratio make these reactions more efficient, which is appealing for progressive catalytic technologies. Hellsing et al [1] created a kinetic model to investigate the platinum catalyst (H_2 + O_2) reaction at high temperatures (~1000 K) and pressures. The model was able to predict reaction kinetics at elevated pressures which would assist in guiding high pressure experiments and improve performance calculations in catalytic combustor applications. Bui [2] examined the catalytic ignition of hydrogen/air mixtures over *Pt* using detailed stagnation-point flow modeling that encompassed gas-phase and surface kinetics as well as transport phenomena. The influence of strain rate, pressure, and preheating on catalytic ignition was also studied. In general, the model results illustrated the intricate interactions of kinetics, transport, and thermal effects during catalytic ignition. A summary is presented in [3]. Numerical simulation studies are performed to investigate the hydrogen-oxygen reaction on platinum catalytic surface with the surface diffusion velocity as the focus of the investigation. The systems were able to maintain stable surface temperatures that were dependent on adsorption and desorption rates, but surface diffusion velocities did not affect temperature control. The study's [4] focus was on catalytic combustion of hydrogen-air mixtures and was completed using numerical simulations of a platinum-coated hot plate. The process was modeled with heat transfer and gas phase chemical reactions (8 species with 24 reactions) and on the platinum surface (additional surface species with 14 reactions). The study noted the effectiveness of catalytic combustion in stabilizing low temperature flames while reducing nitrogen oxides emissions. Boundaries of hydrogen-air mixtures flowing over catalytic platinum hot plates and through rectangular channels was studied computationally in Ref. [5]. The surface reaction, as well as heat and mass transfer, were normalized to develop correlations appropriate for the design of catalytic reactors and porous burners intended for stabilization of low temperature flames that, in turn, reduce emissions like nitrogen oxides. In Ref. [6], a micro combustor design was presented with a three-dimensional combustion model whose flame structure consists of a preheat zone, reaction zone, and post flame zone. This model explains the effects of Peclet

*Corresponding author's email: sab.famech@birjand.ac.ir

number, dimensionality, and asymptotic/non-asymptotic approximations, as well as micro-combustor structural heat conduction (Peclet number). In Ref. [7], A lean hydrogen-air mixture was catalytically combusted in a narrow rectangular channel lined with platinum catalyst. Previous work did a numerical modeling of the surface reaction mechanisms of a catalytic combustion in combination with gas-phase reactions. In Ref. [8], Different depositions of platinum were made on the micro-reactor ZrO_2-supported catalyzers: *Pt,* Pt/Al_2O_3*,* Pt/CeO_2*,* and *Pt/nano-*Al_2O_3. Preferential oxidation of *CO* in the presence of hydrogen was also studied. This research showed that the method of catalyst preparation and the choice of support material profoundly affect the catalytic activity, selectivity, and mass transfer of the catalyst. In Ref. [9] the thermal effects from the exothermic recombination of hydrogen and oxygen and catalytic activity was studied using monometallic (*Pd, Pt*) and bimetallic (*Pd-Pt*) silica and alumina supported catalysts. These results were confirmed with DFT calculations, demonstrating water's interaction with the mono and bimetallic clusters and how that affects their activity and resistance to water poisoning. In Ref.[10], investigated hydrogen peroxide (H_2O_2) synthesis from *H* and *O* in a wall-coated microchannel reactor, direct synthesis catalyzed by *Au–Pd* nanoparticles embedded in a silica wash coat layer. This work showed that the *Au–Pd* catalyst was safe within microchannel technology to process explosive hydrogen-oxygen systems endowed by high efficiency. In Ref. [11] It introduces the surface catalytic reaction within metal microchannel, the system of non-reactive hydrogen-air flow in Ref. [12]. We see that as the hydraulic diameter of the microchannel increases there is a decrease in normalized temperature of mixture and heat transfer to catalyst [12]. Experimental and numerical study of combustion and heat transfer in a micro-reactor fueled with hydrogen, having *SiC* block and platinum channels. In Ref. [12] the micro-reactor (mainly counter-flow geometry), is suggested that could be suitable for power generation applications due to its good microstructural simplicity in (micro) generator units. In Ref. [13], A computational study on flame stability limits of hydrogen/air premixed combustion in planar micro-combustors with catalytic walls for the mitigation of the thermal and radical quenching difficulties in micro-combustion was carried out. Also in this report [14], *Pt-*Al_2O_3 coating for fuel cell off-gas hydrogen to water transfer in polymer electrolyte fuel cells (PEFCs). The findings illustrate the promise of highly super hydrophobic catalyst coatings in microchannel reactors for hydrogen off-gas conversion at PEFCs. In Ref. [15], *SiC*-supported *Pt-Cu* thin films using magnetron sputtering to create catalysts for hydrogen combustion under oxidizing conditions was prepared. The closed-porous sample demonstrated durability over five cycles, highlighting its potential for efficient and stable hydrogen combustion catalysis. In Ref. [16], the combustion and flow characteristics of H_2/O_2 mixtures in a platinum-coated planar microchannel was numerically investigated. The study provided insights into achieving stable flow and combustion in microchannel, offering a theoretical foundation for micro-combustion applications. In Ref. [17] an existing interface model for porous media under local thermal non-equilibrium is extended to investigate heat diffusion from catalytic reactions into fluid, porous solid, and solid wall phases. These results demonstrate that wall thickness has a strong influence on heat and mass transport within the system. In Ref. [18], the medium-temperature shift (MTS) reaction in a microchannel reactor by coating stainless-steel plates with *Ni-K/*CeO_2 catalyst layers using electrophoretic deposition (EPD) was explored. This work highlights the importance of solvent selection in optimizing catalyst deposition and reaction efficiency in microchannel reactors. In Ref. [19], the decomposition of hydrogen peroxide (H_2O_2) on platinum (*Pt*) Nano-catalysts, a cyclic reaction where *Pt* oxidizes to *Pt(O)* and then reduces back to *Pt* was investigated. The work introduced can be applied to calculate rate constants for other reactions involving catalysts cycling between two oxidation states, offering insights into optimizing reaction conditions and catalyst properties for various industrial and technological processes. In Ref. [20], the transport phenomena in micro-reactors, focusing on a single microchannel filled with a porous medium, using both one-dimensional and two-dimensional models with catalytic activity is explored. The study highlights the complex interplay between hydrodynamics and catalytic activity, demonstrating how reflux features influence product distribution in corrugated channels. These findings enhance the understanding and design of micro reactors for chemical synthesis and combustion applications. In Ref. [21] a counter-flow methane/air premixed flame in a plus-shaped burner, comparing its behavior with and without platinum and rhodium catalytic walls was examined. The study demonstrates that platinum significantly affects NO_2 emissions across a range of flame conditions, including lean, stoichiometric, and rich mixtures. In Ref. [22], a high-efficiency methane catalytic combustion burner for hydrogen production using composite catalysts combining spinel CoX_2O_4 (*X = Al, Fe, Cr, Cu*) with hex aluminate is designed. The study demonstrated the benefits of composite catalysts for optimizing methane combustion and hydrogen production. In Ref. [23] the use of quantum computing to improve the efficiency of the oxygen reduction reaction (ORR) on platinum-based surfaces, a key challenge in hydrogen fuel cells is explored. The results highlight the potential of quantum computing to address strongly correlated electronic systems and suggest platinum/cobalt as a promising candidate for future quantum advantage in ORR applications. In Ref. [24, 25] analytical method are used to investigate how different boundary conditions and the thermal and physical properties of walls and gas affect the characteristics and stability of hydrogen-air flames. The results indicate that the maximum gas temperature variation is approximately 6.5 times greater than the wall temperature variation.

Another method used by researchers is the Reconstruction of Variation Iteration Method (RVIM), which is employed as a powerful and suitable algorithm for finding analytical solutions to ordinary or partial differential equations. This method utilizes the Laplace Transform to overcome

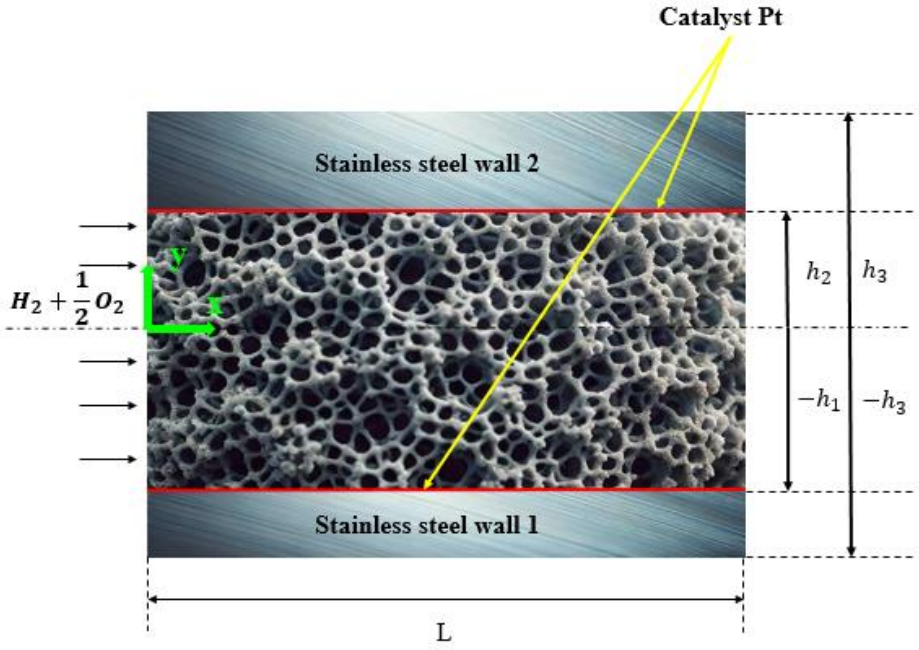

Fig. 1. A microchannel with a porous medium, platinum catalyst plates, and two walls of differing thicknesses.

the difficulties of perturbation techniques or Adomian polynomials, while also reducing the computational load. It is independent of small parameters, making it a novel and efficient technique [26]. Other analytical methods also exist, including the Homotopy Perturbation Method (HPM), which has been used to solve nonlinear equations in articles [27-30]. Additionally, the Akbari-Ganji Method (AGM), a new and efficient semi-analytical approach, has been applied to solve nonlinear equations in articles [29-33].

In this work, the analytical solution [17] has been modified and improved so that it can be used for physical problems and is not limited to the mathematical aspects of the work. The novel study is concentrated to an analytical method low-temperature hydrogen surface reaction within a microporous medium with complete physical description that is not available in before works. This work enables the comprehensive parametric analysis for the design of a novel porous micro-reactor aimed at optimizing the water production process in petrochemical industries and fuel cell components.

2- Model description

2- 1- Physical model

Fig. 1 shows a schematic representation of the microchannel with a porous medium and platinum plates under investigation. The channel features two asymmetric walls, where the thickness of the upper wall (Wall 2) is greater than that of the lower wall (Wall 1). The walls are made of stainless steel, and the porous medium is examined for three materials: alumina (Al_2O_3), titanium dioxide (TiO_2), and silicon carbide (SiC).

Table 1 outlines the specifications of the three cases studied, while Table 2 provides the thermal conductivity properties of the materials investigated in this research. In this channel, hydrogen and oxygen are introduced as reactants into the microchannel. Following the surface reaction of hydrogen and oxygen with the platinum catalyst—an exothermic reaction—water vapor is produced as the final product.

3- Mathematical model and boundary conditions

The governing equations of this problem are included as momentum, energy and mass equations that are written into a micro-porous reactor.

3- 1- Momentum equation

The momentum equation operates under the assumption that the fluid flow is incompressible, steady, and laminar, satisfying the no-slip boundary condition on the walls. The flow is from left to right, as shown in Fig. 1, and is purely axial. Under steady-state conditions and for a fully developed flow, the Darcy-Brinkman momentum equation governs the hydrodynamics of the system. This means that:

$$-\frac{\delta p}{\delta x}+\mu_{eff}\frac{d^2u}{dy^2}-\frac{\mu_f}{\kappa}u=0, \quad -h_1\le y<h_2 \qquad (1)$$

Where μ_f and μ_{eff} represent the fluid viscosity and the effective viscosity of the porous medium, respectively,

Table 1. The specifications of the three cases considered in this study.

Case	Porous medium material	Wall material 1 and 2	
Case 1	Al_2O_3	316-Stainless steel	0.0223377
Case 2	TiO_2	316-Stainless steel	0.0609209
Case 3	SiC	316-Stainless steel	0.067

Table 2. The specifications of the three cases considered in this study.

Material	
Al_2O_3	30
TiO_2	11
SiC	10
316-Stainless steel	15.1

u is the fluid phase velocity, κ is the permeability of the porous medium, $\frac{\partial p}{\partial x}$ is the pressure gradient, and y is the height direction of the microchannel. This microchannel is asymmetric. The equation is applied to the porous region and includes an interface range between the porous medium and the wall. The no-slip boundary conditions at the walls of the microchannel are considered as follows:

$$u = 0, \quad y = -h_1 \tag{2}$$

$$u = 0, \quad y = h_2 \tag{3}$$

3- 2- Energy equation

Axial heat conduction within the wall is negligible and has been ignored in this study. Heat transfer in upper wall, where T_2 and k_2 represent the temperature and thermal conductivity ratio of upper wall, respectively, is governed by the following energy equation:

$$k_2 \frac{\partial}{\partial y}\left[\frac{\partial T_2}{\partial y}\right] = 0, \quad h_2 < y \le h_3 \tag{4}$$

For lower wall, the energy equation is as follows, where T_1 and k_1 represent the temperature and thermal conductivity ratio of lower wall, respectively:

$$k_1 \frac{\partial}{\partial y}\left[\frac{\partial T_1}{\partial y}\right] = 0, \quad -h_3 < y \le -h_1 \tag{5}$$

The porous medium is homogeneous, isotropic, and fully saturated with fluid, and the fluid and solid phases are solved independently without overall averaging; that is, it operates under local thermal non-equilibrium conditions. Additionally, gravitational effects and radiative heat transfer are neglected. Physical properties such as porosity, specific heat, density, and thermal conductivity are assumed to be constant, and radiation effects are ignored. The heat flow is assumed to be fully developed. The energy equations for the solid and fluid phases in the porous medium under local thermal non-equilibrium conditions are expressed as follows:

$$k_{ef}\frac{d^2T_f}{dy^2} + h_{sf}a_{sf}(T_s - T_f) + \frac{\mu_f}{\kappa}u^2 + \mu_{eff}\left(\frac{du}{dy}\right)^2 = \rho_f C_{p,f} u \frac{\partial T}{\partial x}, \quad -h_1 \le y \le h_2 \tag{6}$$

$$k_{es}\frac{d^2T_s}{dy^2}-h_{sf}a_{sf}(T_s-T_f)=0,\qquad -h_1\le y<h_2 \tag{7}$$

In these equations, T_f and k_{ef} represent the temperature and effective thermal conductivity of the fluid phase in the porous medium, respectively. Similarly, T_s and k_{es} represent the temperature and effective thermal conductivity of the solid phase in the porous medium, respectively. The interstitial heat transfer coefficient is denoted by h_{sf} and the specific surface area is represented by a_{sf} while ρ_f is the fluid density and $C_{p,f}$ is the specific heat capacity of the fluid.

The boundary condition at the outer edge of upper wall, the heat flux q''_{w2} is defined as follows:

$$k_2\left.\frac{\partial T_2}{\partial y}\right|_{y=-h_3}=-q''_{w2},\qquad y=h_3 \tag{8}$$

At the interface where the porous medium shares a boundary with upper wall, the coupling requires a constant temperature condition between the phases of the porous medium and the wall itself. Additionally, the heat flux from the catalytic surface q''_c is distributed to the respective phases based on the effective thermal conductivity and temperature gradient.

$$\begin{aligned} q''_c &= k_{ef}\left.\frac{\partial T_f}{\partial y}\right|_{y=h_2}+k_{es}\left.\frac{\partial T_s}{\partial y}\right|_{y=h_2}-k_2\left.\frac{\partial T_2}{\partial y}\right|_{y=h_2} \\ T_2 &= T_f=T_s,\qquad y=h_2 \end{aligned} \tag{9}$$

Similarly, for the interface between the porous medium and lower wall the boundary condition is as follows:

$$\begin{aligned} q''_c &= -k_{ef}\left.\frac{\partial T_f}{\partial y}\right|_{y=h_1}-k_{es}\left.\frac{\partial T_s}{\partial y}\right|_{y=-h_1}-k_1\left.\frac{\partial T_1}{\partial y}\right|_{y=-h_1} \\ T_2 &= T_f=T_s,\qquad y=-h_1 \end{aligned} \tag{10}$$

Additionally, the reaction rate of hydrogen and air on platinum is given by the Schefer equation as follows:

$$q''_c=12040C_M\exp\left(-\frac{1792.1}{T_W}\right) \tag{11}$$

where C_M is the molar density of hydrogen-air mixture and T_W is the wall temperature, which here is 300 K. Finally, at the outer edge of lower wall, the heat flux q''_{w1} is defined as:

$$k_1\left.\frac{\partial T_1}{\partial y}\right|_{y=-h_3}=-q''_{w1},\qquad y=-h_3 \tag{12}$$

3- 3- Mass concentration equation

The chemical reactions related to the hydrogen-air reaction on the platinum catalyst occur as surface reactions on both lower and upper wall. Considering this, the mass transport equation for the chemical species is as follows:

$$u\frac{\partial C_i}{\partial x}=D\frac{\partial^2 C_i}{\partial y^2}+D_T\frac{d^2T_f}{dy^2},\qquad 0\le y<h_1 \tag{13}$$

where C is the concentration, D is the mass diffusion coefficient, and D_T is the thermal mass diffusion coefficient. The boundary conditions associated with the mass equation are as follows:

$$D\left.\frac{\partial C}{\partial y}\right|_{h_2}=k_R(C-C_b),\qquad y=h_2 \tag{14}$$

$$D\frac{\partial C}{\partial y}=D_T\frac{\partial T_f}{\partial y},\qquad y=\frac{h_2-h_1}{2} \tag{15}$$

$$C(0,y)=C_0,\qquad x=0 \tag{16}$$

4- Normalization and final solution

To solve some of the governing equations, they must be converted into dimensionless forms. This is achieved by defining a series of dimensionless parameters. The parameters listed in Table 3 are introduced to further simplify the physical analysis. To clarify the process of solving the equations and continuity in this work, the complete path for solving the momentum, energy, and concentration equations is illustrated in the flowchart below.

To obtain the velocity distribution using dimensionless parameters, we first normalized Eq. (1) as follows:

$$M\frac{d^2U}{dY^2}-\frac{U}{Da}+1=0,\qquad -Y_1\le Y\le Y_2 \tag{17}$$

In this equation, $\mu_{eff}=\mu_f$ is assumed. Now, the dimensionless equation is solved under the following dimensionless boundary conditions:

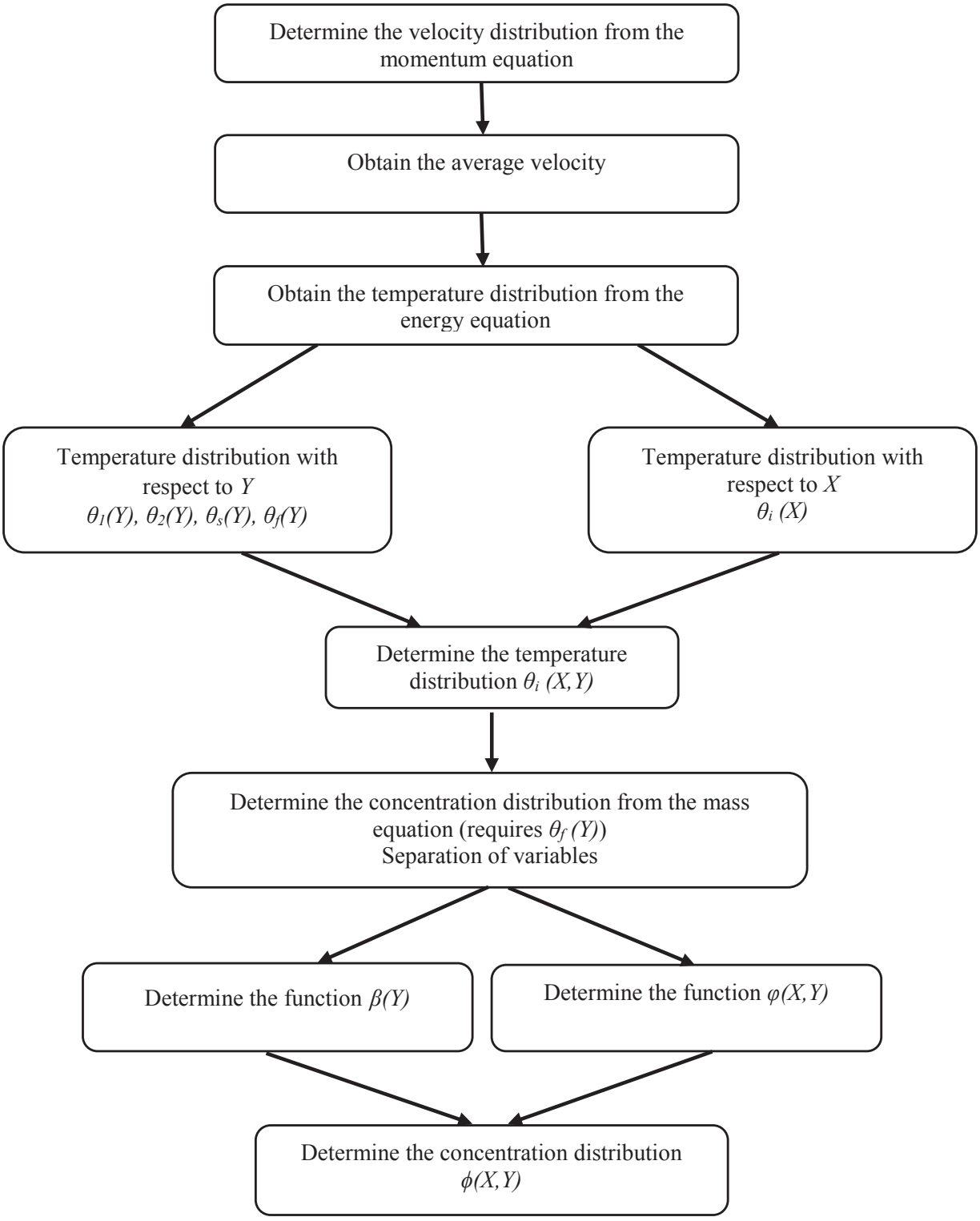

Fig. 2. Flowchart illustrating the solution procedure for the momentum, energy, and concentration equations.

Table 3. Definition of dimensionless parameters.

$\theta_i = \frac{(T_i - T_{w,in})k_{es}}{(q_1^{"} + q_2^{"})h_3}$	$U = \frac{u}{u_r}$	$S = \frac{1}{\sqrt{M\,Da}}$	$k_{e1} = \frac{k_1}{k_{es}}$
$Y = \frac{y}{h_3}$	$X = \frac{x}{L}$	$\Pr = \frac{C_{p,f}\mu_{eff}}{k_{ef}}$	$k_{e2} = \frac{k_2}{k_{es}}$
$Y_1 = \frac{h_1}{h_3}$	$u_r = -\frac{h_2^2}{\mu_f}\frac{\partial p_f}{\partial x}$	$q_1^{"} = q_c^{"} - q_{w1}^{"}$	$Q_{w1} = \frac{q_{w1}^{"}}{(q_1^{"} + q_2^{"})}$
$Y_2 = \frac{h_2}{h_3}$	$Da = \frac{\kappa}{h_2^2}$	$q_2^{"} = q_c^{"} - q_{w2}^{"}$	$Q_{w2} = \frac{q_{w2}^{"}}{(q_1^{"} + q_2^{"})}$
$\xi = \frac{h_3}{L}$	$M = \frac{\mu_{eff}}{\mu_f}$	$\gamma = \frac{k_R(h_1 + h_2)}{D\,C_0}$	$Q = \frac{q_2^{"}}{(q_1^{"} + q_2^{"})}$
$k = \frac{k_{ef}}{k_{es}} = \frac{\varepsilon k_f}{(1-\varepsilon)k_s}$	$\mathrm{Re} = \frac{h_3\,\rho_f \overline{u}}{\mu_{eff}}$	$Br^{'} = \frac{\mu_{eff}\overline{u}^2}{(q_1^{"} + q_2^{"})h_3}$	$Sr = \frac{(q_1^{"} + q_2^{"})(h_1 + h_2)D_T}{C_0 k_f D}$
$Bi = \frac{h_{sf}a_{sf}h_3^2}{k_{es}}$	$\phi = \frac{C}{C_0}$		

$$U(-Y_1) = U(Y_2) = 0 \tag{18}$$

The general solution to Eq. (17), i.e., the dimensionless velocity distribution in the microchannel, is obtained as follows:

$$U(Y) = A_1 \cosh(SY) + A_2 \sinh(SY) + Da \tag{19}$$

Given the assumption of fully developed flow and considering the stated assumptions, the following conditions hold:

$$\frac{\partial T_f}{\partial x} = \frac{\partial \overline{T}_f}{\partial x} = \frac{\partial T_s}{\partial x} = \frac{\partial \overline{T}_s}{\partial x} = \frac{\partial T_{w1}}{\partial x} = \frac{\partial T_{w2}}{\partial x} = \Omega = cons\tan t. \tag{20}$$

Here, we seek a solution for the temperature distribution by solving the thermal equations in the following form:

$$T_i = f_i(y) + \Omega x, \qquad i = 1, 2, s, f \tag{21}$$

Where $f_i(y)$ is a function determined by solving Eq. (6) and Eq. (7) and applying the boundary conditions described in Eq. (8) to Eq. (12) . To obtain the temperature distribution in the x direction, we first substitute the second term of Eq. (6) into Eq. (7) and then integrate Eq. (6) to arrive at Eq. (22).

$$q_1^{"} + q_2^{"} + \frac{\mu_f}{\kappa}\int_{-h_1}^{h_2} u^2 dy + \mu_{eff}\int_{-h_1}^{h_2} (\frac{du}{dy})^2 dy = \rho_f C_{p,f}\int_{-h_1}^{h_2} u\frac{\partial T_f}{\partial x} dy \tag{22}$$

Now, using the velocity distribution equation, $\frac{\partial T_f}{\partial x}$ which is equivalent to the constant Ω and the unknown in the above equation, is obtained through manual solution as follows:

$$\frac{\partial \overline{T}_f}{\partial x} = \frac{A_4\overline{u}^2\mu_{eff} + 2h_3(q_1^{"} + q_2^{"})}{\overline{u}\,\rho_f C_{p,f}(h_1 + h_2)h_3} = \Omega \tag{23}$$

Table 4. The default values of the dimensionless parameters used in the figures.

Dimensionless parameter	Value	Dimensionless parameter	Value
Sr	66.73	ε	0.95
γ	29.52	Pe	51.56
Q	0.529	Br'	$1.33 * 10^{-8}$
Q_{w1}	0.2353	Da	0.1
Q_{w2}	0.17647	Pr	1.2332
Y_1	0.9	Re	300
Y_2	0.8	ξ	0.05

Where the bulk mean temperature of the fluid is obtained as follows:

$$\overline{T}_f = \frac{1}{\overline{u}(h_1+h_2)}\int_{-h_1}^{h_2} uT_f dy \tag{24}$$

Now, the axial temperature distribution can be determined by applying Eq. (20)-(23) and subsequently normalizing the resulting differential equation. Solving the resulting equation in a way that satisfies the solution of Eq. (21), the dimensionless temperature θ_i in the dimensionless axial direction X is obtained as:

$$\theta_i(X) = \frac{X(1+Br'A_4)}{\mathrm{Re}\,\mathrm{Pr}\,k(Y_1+Y_2)\xi}, \qquad i=1,2,s,f \tag{25}$$

Where Br' ,Re, Pr, ξ represent the modified Brinkman number, Reynolds number, Prandtl number, and the aspect ratio of the microchannel, respectively. The default values of the dimensionless parameters are provided in Table 4.

The dimensionless forms of Eq. (8)-(12) are obtained through algebraic manipulation and by substituting the parameters listed in Table 1, along with using Eq. (20) and Eq. (23), to derive the dimensionless energy equation for Wall 2.

$$k_{e2}\theta_2'' = 0, \quad Y_2 < Y \le 1 \tag{26}$$

The dimensionless energy equations in the porous medium are expressed as:

$$k\theta_f'' + Bi(\theta_s-\theta_f) + B_1\cosh(2SY) + B_2\cosh(SY) + B_4\sinh(SY) + B_5 = 0, \quad -Y_1 \le Y < Y_2 \tag{27}$$

$$\theta_s'' + Bi(\theta_s-\theta_f) = 0, \quad -Y_1 \le Y < Y_2 \tag{28}$$

Where Bi is the Biot number, as defined in Table 3. The dimensionless energy equation for Wall 1 is:

$$k_{e1}\theta_1'' = 0, \quad -1 \le Y < -Y_1 \tag{29}$$

This completes the 12 boundary conditions needed to close the system, as summarized in Table 5. In this table, Q_{w1} and Q_{w2} represent the dimensionless heat flux ratios at the outer edges of Wall 1 and Wall 2, respectively. Applying the boundary conditions provided in Table 5 enables analytical solutions to the system of Eq. (26) -(29) to be found.

The Nusselt number represents the ratio of convective to conductive heat transfer occurring at the interface between the walls and the porous fluid phase. The heat transfer coefficients at the lower and upper walls of the microchannel are defined as follows:

$$H_1 = \frac{q_1''}{T_1 - \overline{T}_f} \tag{30}$$

$$H_2 = \frac{q_2''}{T_2 - \overline{T}_f} \tag{31}$$

Table 5. Boundary conditions for closing the system.

$\theta_f(-Y_1)=\theta_s(-Y_1)=0,$	$\theta_f(Y_2)=\theta_s(Y_2)=\theta_{w2}$
$\theta_s^{"}(-Y_1)=\theta_s^{"}(Y_2)=0,$	$\theta_1(-Y_1)=0, \quad \theta_2(Y_2)=\theta_{w2}$
$k_{e1}\theta_1^{'}(-1)=Q_{w1},$	$k_{e2}\theta_2^{'}=-Q_{w2}$
$\theta_f^{"}(-Y_1)=-\frac{1}{k}[B_1\cosh(2SY_1)-B_2\sinh(2SY_1)+B_3\cosh(SY_1)-B_4\sinh(SY_1)+B_5]$	
$\theta_f^{"}(Y_2)=-\frac{1}{k}[B_1\cosh(2SY_2)+B_2\sinh(2SY_2)+B_3\cosh(SY_2)+B_4\sinh(SY_2)+B_5]$	

Therefore, the Nusselt number, using the height of the microchannel (h_1+h_2) as the characteristic length, and Eq. (30) and Eq. (31), which define the heat transfer coefficients and k_{ef} as the effective thermal conductivity of the fluid phase, is normalized as follows:

$$Nu_1=\frac{H_1(h_1+h_2)}{k_{ef}}=\frac{(Q-1)(Y_1+Y_2)}{k\bar{\theta}_f} \tag{32}$$

$$Nu_2=\frac{H_2(h_1+h_2)}{k_{ef}}=\frac{Q(Y_1+Y_2)}{k(\theta_{w2}-\bar{\theta}_f)} \tag{33}$$

The average dimensionless bulk temperature of the fluid, $\bar{\theta}_f$ can be found by normalizing Eq. (24) and then integrating it across the microchannel as follows:

$$\bar{\theta}_f=\frac{A_3}{(Y_1+Y_2)}\int_{-Y_1}^{Y_2}\theta_f[A_1\cosh(SY)+ \tag{34}$$

$$A_2\sinh(SY)+Da]dY$$

To solve the concentration equation using the method of separation of variables. Finally, using the dimensionless parameters in Table 3, Eq. (13) are normalized as follows:

$$\frac{u}{L}\frac{\partial\varphi}{\partial X}=\frac{D}{h_3^2}\frac{\partial^2\varphi}{\partial Y^2} \tag{35}$$

$$\beta^{"}(Y)+\frac{Sr.k}{\varepsilon(Y_1+Y_2)}\theta_f^{"}(Y)=0 \tag{36}$$

The boundary conditions associated with Eq. (36) are normalized as follows:

$$\beta^{'}(Y_2)=\frac{k_R h_3}{D}\beta(Y_2) \tag{37}$$

$$\beta^{'}(\frac{Y_2-Y_1}{2})=\frac{Sr.k}{\varepsilon(Y_1+Y_2)}\theta_f^{'}(\frac{Y_2-Y_1}{2}) \tag{38}$$

The Sherwood number is a dimensionless parameter that describes the ratio of convective mass transfer to molecular mass transfer. This number is very important in microchannel systems for evaluating mass transfer performance in porous environments. Since the reaction occurring on the catalyst surface is of zero order, the reaction rate is not dependent on the concentration of reactants or products (as long as there is sufficient reactant to sustain the reaction). Therefore, the mass transfer coefficient H_m is calculated according to the following relation:

$$H_m=\frac{k_R}{C_0-\bar{C}} \tag{39}$$

With the mass transfer coefficient H_m defined in this manner, and using the microchannel height (h_1+h_2) as the characteristic length scale, the Sherwood number can be expressed as follows and converted into dimensionless terms:

$$Sh=\frac{(h_1+h_2)H_m}{D}=\frac{\gamma}{D(1-\bar{\phi})} \tag{40}$$

Where the dimensionless volumetric concentration, $\bar{\phi}$ is found in a manner similar to Eq. (38).

$$\bar{\phi}=\frac{A_3}{(Y_1+Y_2)}\int_{-Y_1}^{Y_2}\phi[A_1\cosh(SY)+ \tag{41}$$

$$A_2\sinh(SY)+Da]dY$$

The dimensionless temperature formulas in closed form along the height of the microchannel are as follows:

Dimensionless temperature in Wall 2:

$$\theta_2(Y) = C_1 + C_2 Y, \qquad -Y_2 \le Y < 1 \tag{42}$$

Dimensionless temperature of the porous solid phase:

$$\theta_s(Y) = C_3\cosh(2SY) + C_4\cosh(SY) + C_5\cosh(\alpha Y) \tag{43}$$
$$+ C_6\sinh(2SY) + C_7\sinh(SY)$$
$$+ C_8\sinh(\alpha Y) + C_9 Y^2 + C_{10} Y + C_{11}, \quad -Y_1 \le Y < Y_2$$

Dimensionless temperature of the porous fluid phase:

$$\theta_f(Y) = C_{12}\cosh(2SY) + C_{13}\cosh(SY) + C_{14}\cosh(\alpha Y) \tag{44}$$
$$+ C_{15}\sinh(2SY) + C_{16}\sinh(SY)$$
$$+ C_{17}\sinh(\alpha Y) + C_{18} Y^2 + C_{19} Y + C_{20}, \quad -Y_1 \le Y < Y_2$$

And the dimensionless temperature in Wall 1:

$$\theta_1(Y) = C_{21} + C_{22} Y, \qquad -1 \le Y < -Y_1 \tag{45}$$

Substituting Eq. (25) and Eq. (42)-(45) into Eq. (21) yields the final temperature distributions as follows:

Dimensionless temperature distribution in Wall 2:

$$\theta_2(X,Y) = \frac{X(1+Br' A_4)}{\mathrm{Re}\,\mathrm{Pr}.k(Y_1+Y_2)\xi} + C_1 + C_2 Y, \quad -Y_2 \le Y < 1 \tag{46}$$

Dimensionless temperature distribution in the solid phase of the porous medium:

$$\theta_s(X,Y) = \frac{X(1+Br' A_4)}{\mathrm{Re}\,\mathrm{Pr}.k(Y_1+Y_2)\xi} + C_3\cosh(2SY) + C_4\cosh(SY) \tag{47}$$
$$+ C_5\cosh(\alpha Y) + C_6\sinh(2SY)$$
$$+ C_7\sinh(SY) + C_8\sinh(\alpha Y) + C_9 Y^2 + C_{10} Y + C_{11}, \quad -Y_1 \le Y < Y_2$$

Dimensionless temperature distribution in the fluid phase of the porous medium:

$$\theta_f(X,Y) = \frac{X(1+Br' A_4)}{\mathrm{Re}\,\mathrm{Pr}.k(Y_1+Y_2)\xi} + C_{12}\cosh(2SY) + \tag{48}$$
$$C_{13}\cosh(SY) + C_{14}\cosh(\alpha Y)$$
$$+ C_{15}\sinh(2SY) + C_{16}\sinh(SY) + C_{17}\sinh(\alpha Y) +$$
$$C_{18} Y^2 + C_{19} Y + C_{20}, \quad -Y_1 \le Y < Y_2$$

And the dimensionless temperature distribution in Wall 1:

$$\theta_1(X,Y) = \frac{X(1+Br' A_4)}{\mathrm{Re}\,\mathrm{Pr}.k(Y_1+Y_2)\xi} + \tag{49}$$
$$C_{21} + C_{22} Y, \quad -1 \le Y < Y_1$$

Finally, the function $\phi(X, Y)$ is obtained as follows:

$$\phi(X,Y) = \sum C_3 \exp\left(-\frac{LD}{uh_3^2}\lambda^2 X\right).(C_1\sin(\lambda Y) + C_2\cos(\lambda Y)) \tag{50}$$

5- Results and discussion

In this paper, an analytical model of hydrogen/oxygen surface reactions in three different microporous media: alumina (Al_2O_3), titanium dioxide (TiO_2), and silicon carbide (SiC). To solve this problem, the governing equations for momentum, energy, and mass concentration are solved analytically by considering the surface reaction rate and matching conditions at the fluid, porous solid, and solid wall boundaries. In the solution process, the velocity profile is first calculated by solving the momentum equation, and then, by substituting the effects of this distribution into the energy and mass concentration equations, the thermal and mass parameters are obtained.

In fig. 3 illustrates the effect of the porous medium material on the fluid phase normalized temperature contours for three types of alumina (Al_2O_3), titanium dioxide (TiO_2), and silicon carbide (SiC) materials, with 95% porosity. Due to the high thermal conductivity of alumina, it is observed that the temperature gradient in the microchannel is lower. This is attributed to alumina's superior ability to rapidly transfer heat and distribute it more uniformly. As a result, the temperature contours for alumina appear smoother and exhibit gentler variations. Additionally, the average temperature in the microchannel with alumina as the porous medium is slightly higher compared to the other two cases, as heat is distributed more effectively throughout the medium. Among the three selected micro-porous media, Silicon carbide and alumina respectively exhibit the lowest and highest average normalized fluid temperature of 0.5 and 0.15.

Fig. 4 also demonstrates the influence of the porous medium material on the fluid phase normalized temperature contours for three types of alumina (Al_2O_3), titanium dioxide (TiO_2), and silicon carbide (SiC) materials, with 95% porosity. In this figure, alumina, due to its high thermal conductivity, exhibits the lowest temperature gradient in the microchannel.

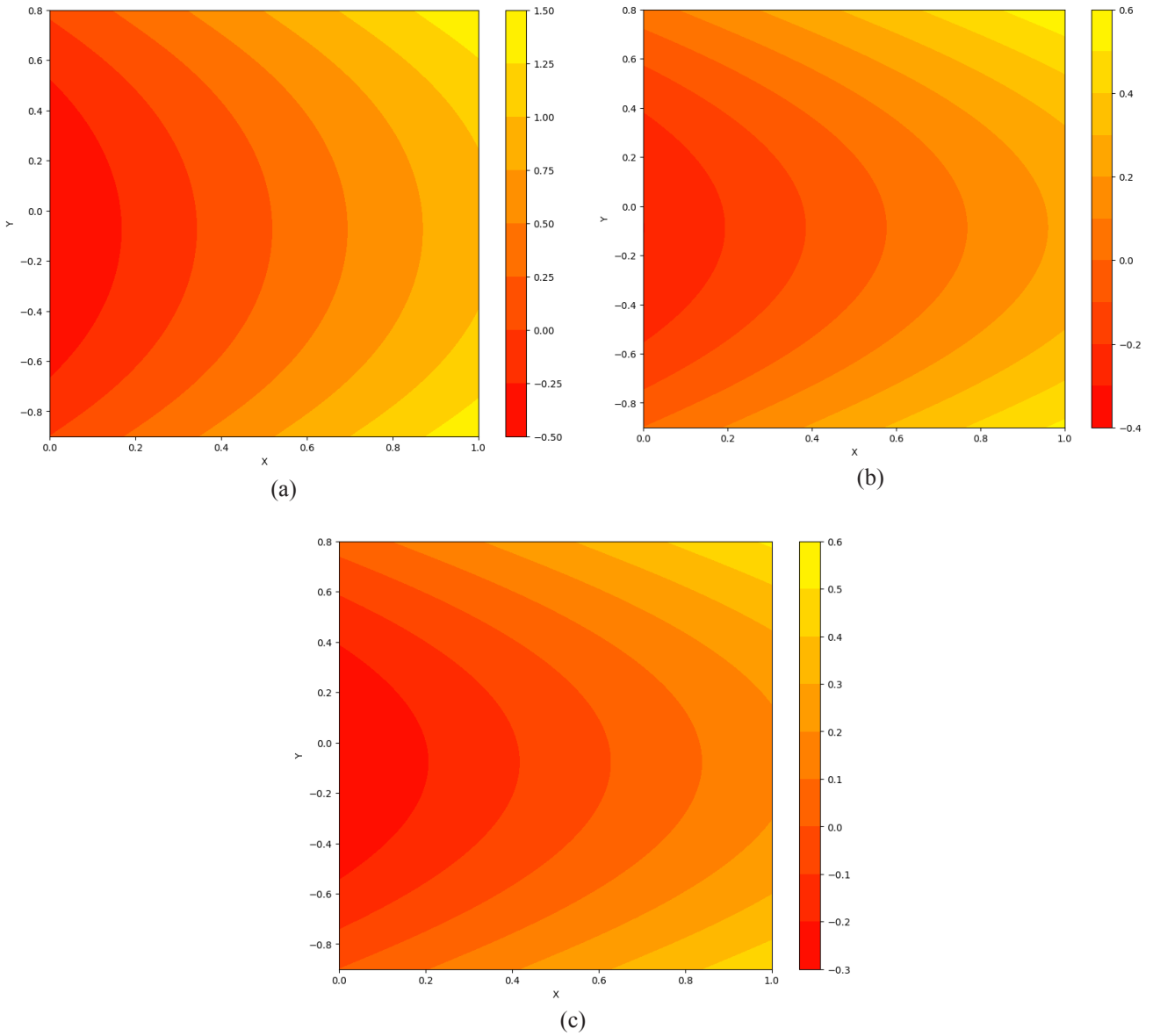

Fig. 3. The effect of the porous medium material on the dimensionless temperature contours of the fluid phase with 95% porosity: a) Al_2O_3, b) TiO_2, c) SiC.

Additionally, alumina facilitates faster heat transfer and provides a more uniform temperature distribution. Silicon carbide and titanium dioxide, owing to their lower thermal conductivity, display higher temperature gradients compared to alumina and perform less effectively in heat transfer. However, when comparing the two medium, silicon carbide has the highest temperature gradient and the lowest average temperature. Among the three selected micro-porous media, Silicon carbide and alumina respectively exhibit the lowest and highest average normalized solid temperature of 0.15 and 0.6.

Fig. 5 illustrates the variation of the Nusselt number at the lower wall against changes in the thickness of the lower and upper walls, ranging from 0.1 to 0.9, for three types of porous media: alumina (Al_2O_3), titanium dioxide (TiO_2), and silicon carbide (SiC), with 95% porosity. In general, for both cases (a) and (b), as the wall height increases, the Nusselt number increases linearly. Alumina, which exhibits the highest Nusselt number across all thickness variations, demonstrates superior heat transfer performance among the three porous media types. Titanium dioxide and silicon carbide have lower Nusselt numbers compared to alumina, with silicon carbide having the lowest. Comparing parts (a) and (b) of the figure, it is observed that the Nusselt number at the lower wall is higher when the dimensionless channel height Y_2 is varied compared to Y_1, which is due to the asymmetry of the microchannel. The

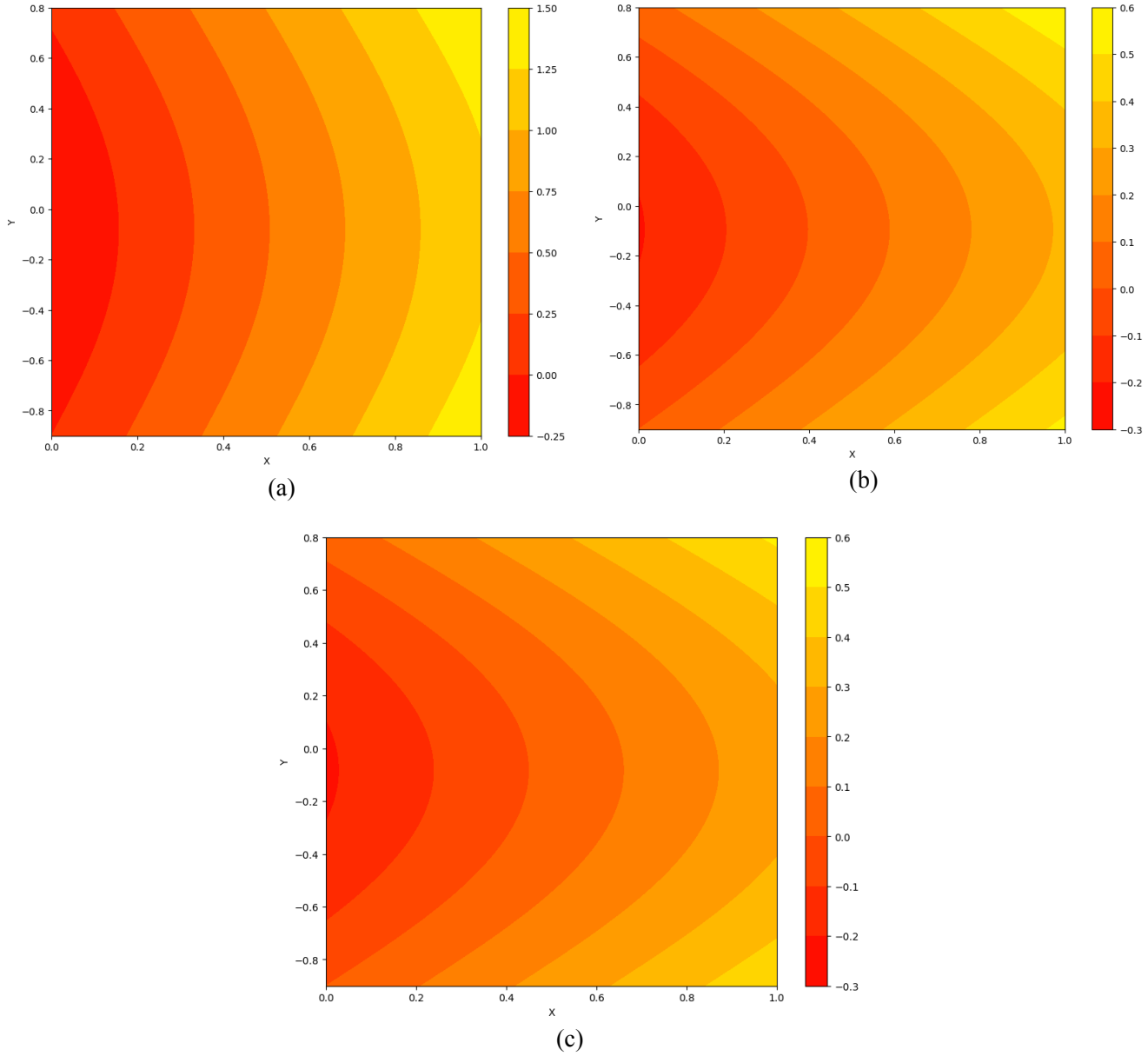

Fig. 5. The effect of the porous medium material on the dimensionless temperature contours of the solid phase with 95% porosity: a) Al_2O_3, b) TiO_2, c) SiC.

maximum variation in the lower Nusselt number with respect to the microchannel width is observed for the alumina porous medium, with values of 58.70% and 53.06% in the lower and upper directions, respectively.

Fig. 6 shows the variation of the Nusselt number at the upper wall against changes in the thickness of the lower and upper walls, ranging from 0.1 to 0.9, for three types of porous media alumina (Al_2O_3), titanium dioxide (TiO_2), and silicon carbide (SiC), with 95% porosity. As the channel height increases, the Nusselt number increases linearly. Alumina still exhibits the highest Nusselt number among the three cases, while silicon carbide has the lowest heat transfer performance. In this context, alumina shows a steeper slope in the variation of the Nusselt number compared to silicon carbide and titanium dioxide. The upper Nusselt number varies with microchannel width by a maximum of 55.31% and 52% in the lower and upper directions, respectively.

Fig. 7 illustrates the variation of the Nusselt number at the lower wall against changes in the thickness of the lower and upper walls, ranging from 0.1 to 0.9, for three types of porous media: alumina (Al_2O_3), titanium dioxide (TiO_2), and silicon carbide (SiC), with 90% porosity. In general, for both cases (a) and (b), as the wall height increases, the Nusselt number increases linearly. Alumina, which exhibits the highest

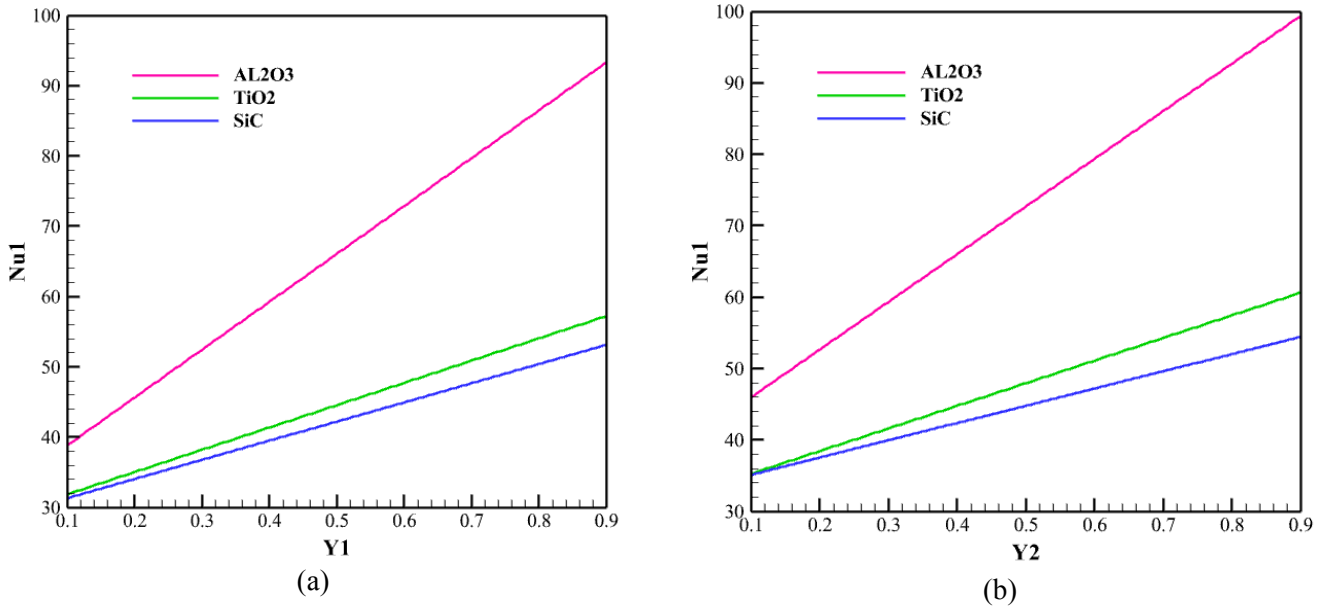

Fig. 6. Variation of the Nusselt number at the upper wall against changes in the thickness of: a) the lower wall and b) the upper wall, with 95% porosity.

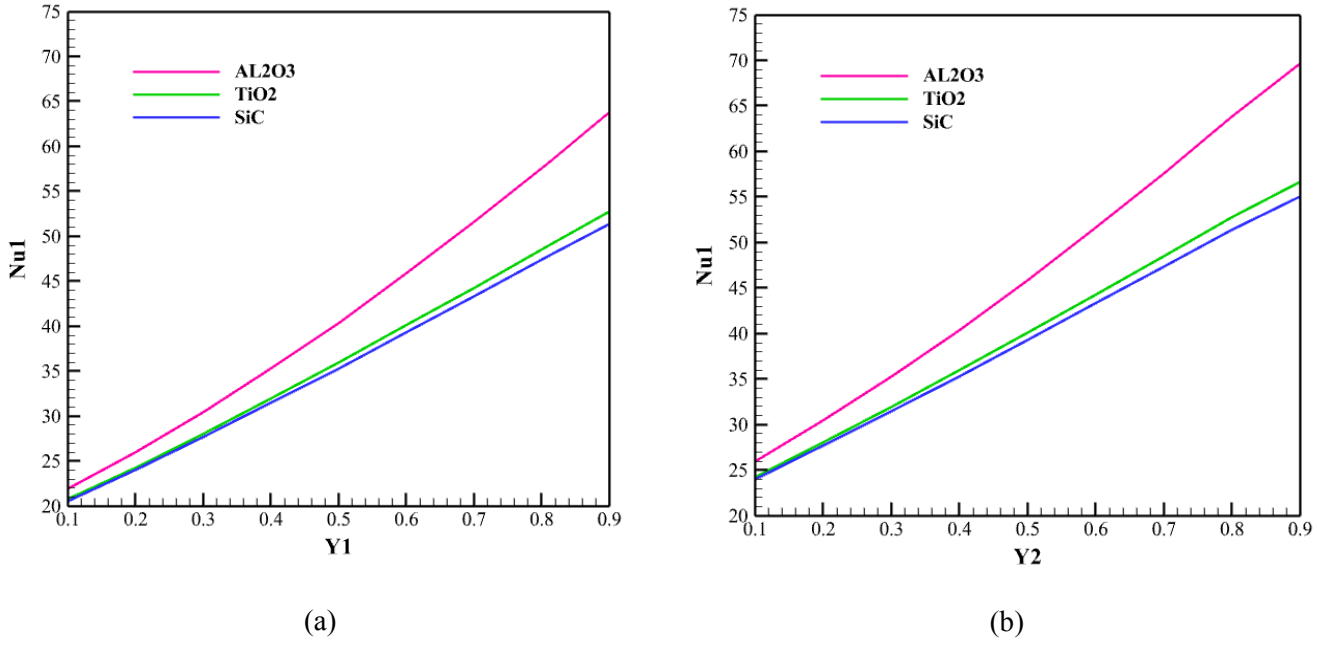

Fig. 7. Variation of the Nusselt number at the lower wall against changes in the thickness of: a) the lower wall and b) the upper wall, with 90% porosity.

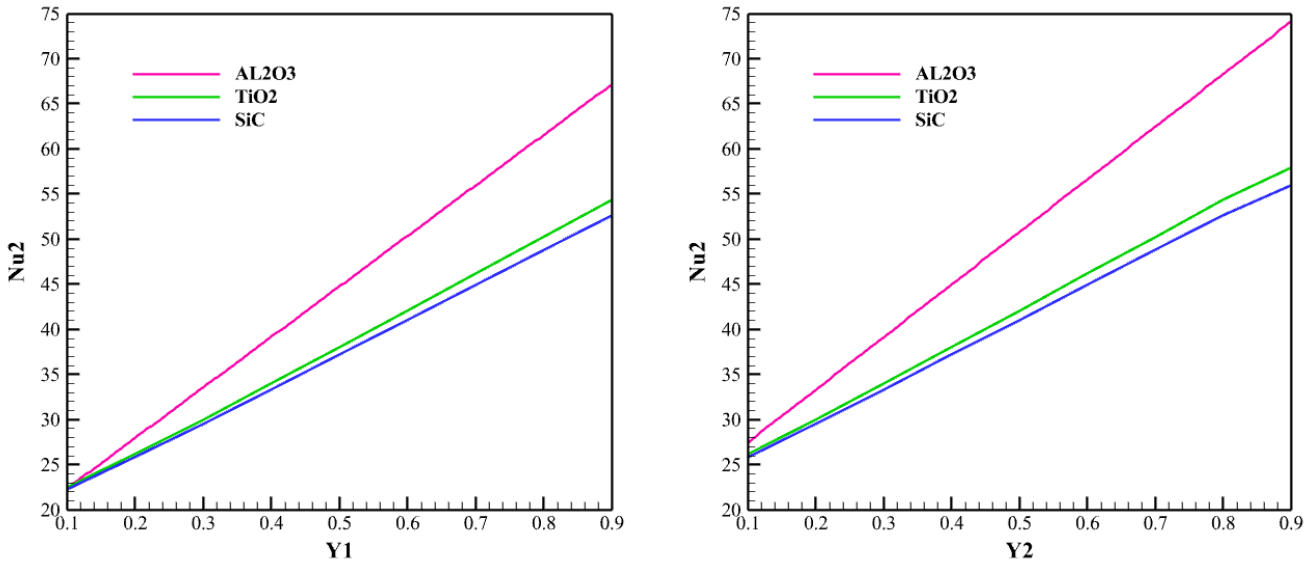

Fig. 8. Variation of the Nusselt number at the upper wall against changes in the thickness of: a) the lower wall and b) the upper wall, with 90% porosity.

Nusselt number across all thickness variations, demonstrates superior heat transfer performance among the three porous media types. Titanium dioxide and silicon carbide have lower Nusselt numbers compared to alumina, with silicon carbide having the lowest. Comparing parts (a) and (b) of the figure, it is observed that the Nusselt number at the lower wall is higher when the dimensionless channel height Y_2 is varied compared to Y_1, which is due to the asymmetry of the microchannel. The maximum variation of lower Nusselt number relative to width of micro-channel is concerned to Alumina porous medium respectively equal to 67.69% and 62.86% for lower and upper directions.

Fig. 8 also shows the variation of the Nusselt number at the upper wall against changes in the thickness of the lower and upper walls, ranging from 0.1 to 0.9, for three types of porous media: alumina (Al_2O_3), titanium dioxide (TiO_2), and silicon carbide (SiC), with 90% porosity. As the channel height increases, the Nusselt number increases linearly. Alumina still exhibits the highest Nusselt number among the three cases, while silicon carbide has the lowest heat transfer performance. In this context, alumina shows a steeper slope in the variation of the Nusselt number compared to silicon carbide and titanium dioxide. Similar to the previous cases, the Nusselt number at the upper wall is higher when the dimensionless height Y_2 is varied compared to Y_1, which is due to the asymmetry of the microchannel. The maximum variation of lower Nusselt number relative to width of micro-channel is concerned to Alumina porous medium respectively equal to 65.15% and 62.16% for lower and upper directions.

Additionally, by comparing Fig. 5 with Fig. 7 and Fig. 6 with Fig. 8, it is observed that as the porosity decreases, the Nusselt number also decreases. In both cases, the Nusselt number increases with increasing wall thickness, but the Nusselt number for 95% porosity is significantly higher than that for 90% porosity. This indicates that heat transfer is more efficient in the higher porosity of medium. The steeper slope at 95% porosity suggests that as the wall thickness increases, the improvement in heat transfer is more pronounced in this medium. This may be due to increased fluid flow and better heat distribution in the higher porosity medium. Furthermore, the variation of Nusselt number versus micro-channel width is increased by decreasing the medium porosity from 95% to 90%.

As shown in Fig. 9, section (a), in the alumina porous medium, the hydrogen concentration decreases rapidly, indicating the rapid consumption of hydrogen in the reaction. This is due to the high thermal conductivity of alumina, which leads to more uniform heat distribution and improved mass transfer. As a result, the reaction occurs more efficiently, and hydrogen is consumed faster. The hydrogen concentration contours for alumina show a steeper gradient, indicating a rapid decrease in hydrogen concentration along the microchannel. Section (b) of Fig. 9 shows that in the titanium dioxide porous environment, hydrogen consumption is slower than in alumina but faster than in silicon carbide. The lower thermal conductivity of titanium dioxide results in less optimal heat distribution and mass transfer, but the reaction still occurs relatively efficiently. The hydrogen

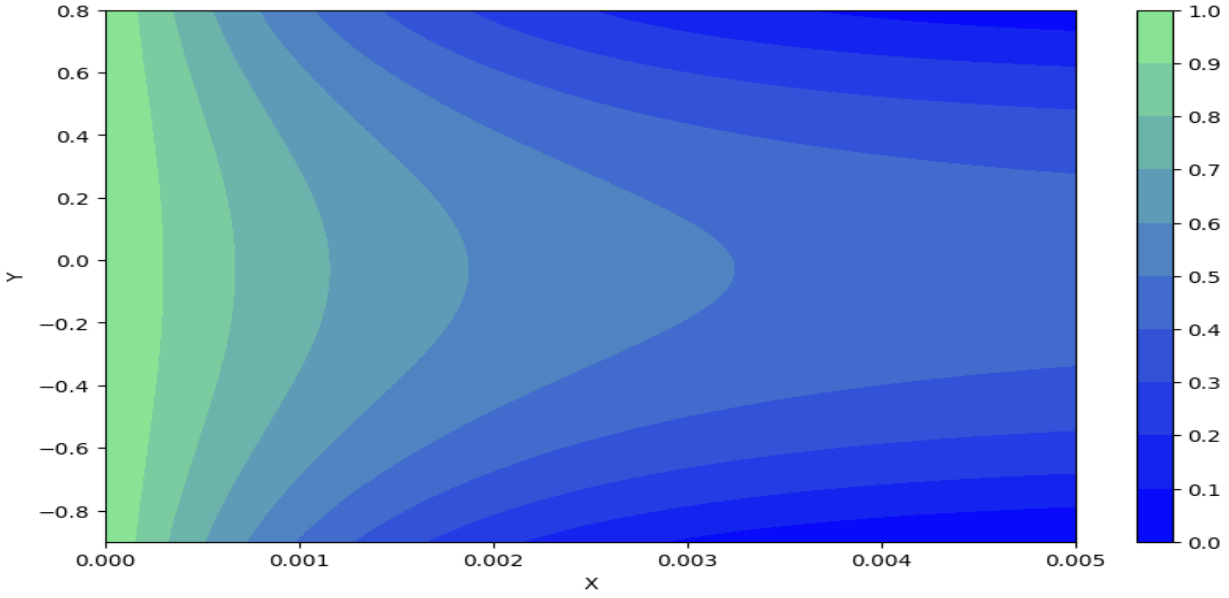

(a)

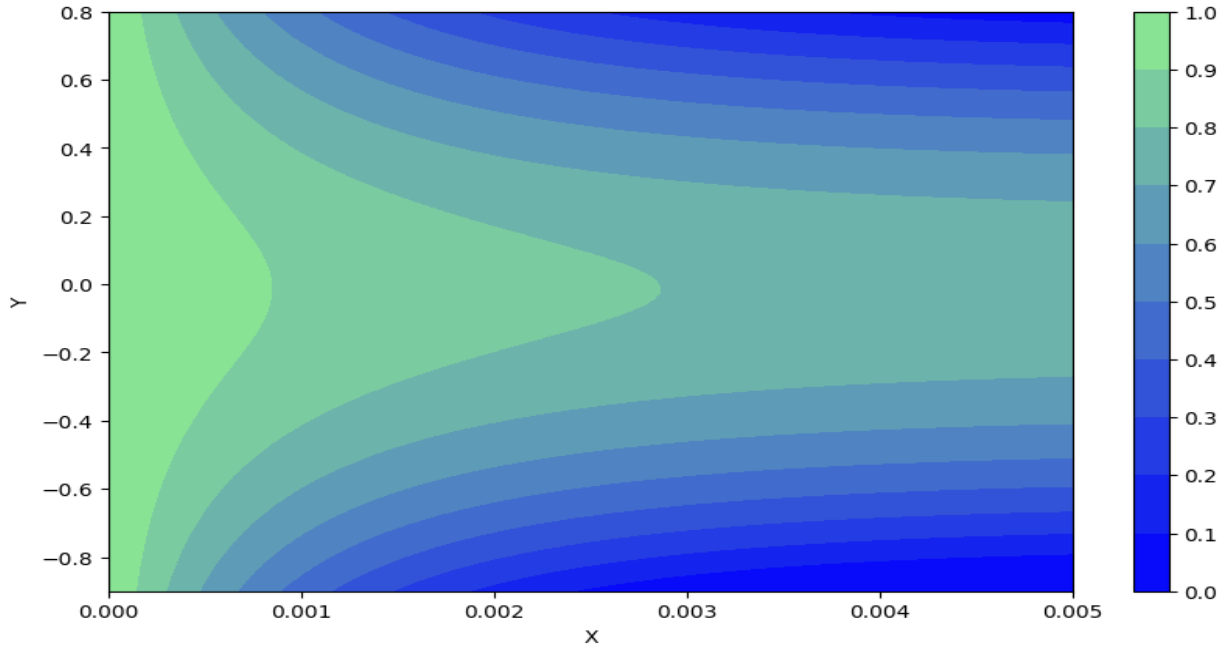

(b)

Fig. 9. The effect of the porous medium type on the hydrogen concentration contours: a) Al_2O_3, b) TiO_2, c) SiC with 95% porosity.(Continued)

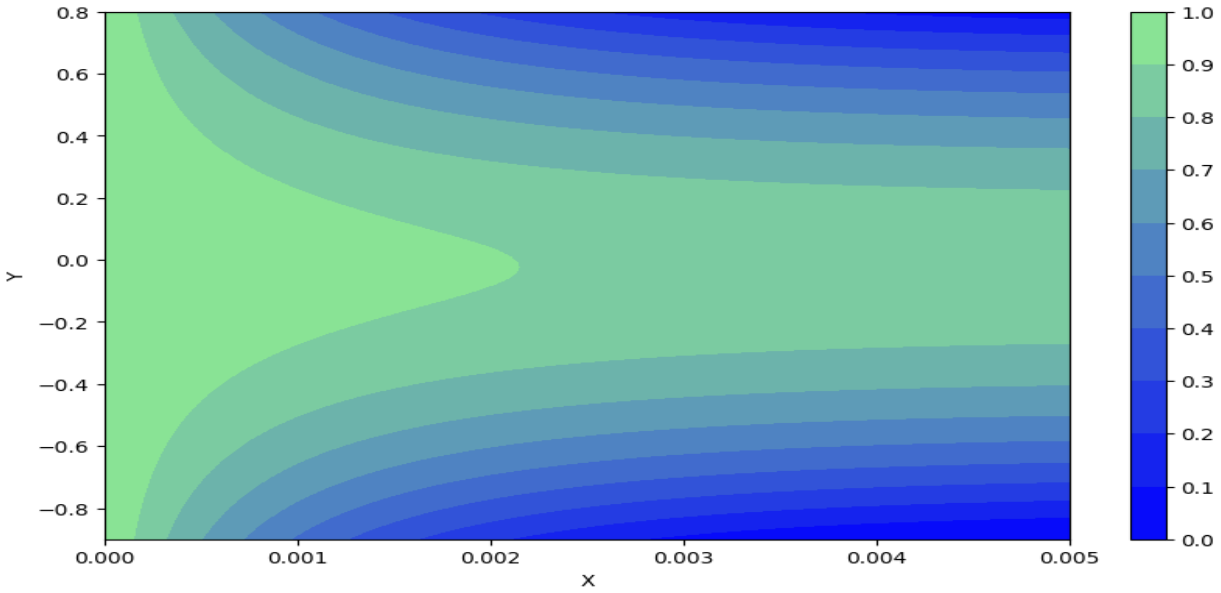

(c)

Fig. 9. The effect of the porous medium type on the hydrogen concentration contours: a) Al_2O_3, b) TiO_2, c) SiC with 95% porosity.

concentration contours for titanium dioxide show a gentler slope compared to alumina, but a noticeable decrease in hydrogen concentration is still observed. Section (c) of Fig. 9 shows that in the silicon carbide porous environment, the least hydrogen consumption is observed.

The low thermal conductivity of silicon carbide results in suboptimal heat distribution and mass transfer, leading to a slower reaction rate and slower hydrogen consumption. The hydrogen concentration contours for silicon carbide show a much gentler slope, indicating slower consumption of hydrogen concentration along the microchannel. The rate of hydrogen to water conversion in alumina media is approximately 41% faster than titanium oxide and 67% faster than silicon carbide.

Fig. 10 shows the variation of the Sherwood number against the change in the thickness of the lower and upper walls for the base case (95% porosity). For both figures, the Sherwood number increases with the increase in channel height thickness, indicating that the increase in channel height improves mass transfer because more space is provided for fluid flow and interaction with the porous medium. The Sherwood number for alumina is the lowest among the three porous environments. This is due to the high thermal conductivity of alumina, which leads to more uniform temperature distribution and reduced concentration gradients. As a result, convective mass transfer is less, and the Sherwood number is lower. The Sherwood number for titanium dioxide and silicon carbide is higher than that of alumina. This is due to their lower thermal conductivity, which causes sharper concentration gradients and increased convective mass transfer. The Sherwood number for alumina increases with the increase in channel height thickness, but the slope of this increase is the lowest among the three porous environments. This indicates that alumina maintains relatively uniform mass transfer even with increased height. The Sherwood number for titanium dioxide also increases with the increase in channel height thickness, but the slope of this increase is higher than that of alumina. Comparing Fig. 10(a) and (b), it is find that the Sherwood number on the upper wall is slightly higher than the lower wall, which is due to the asymmetry in the position of the two walls. The maximum variation in the Sherwood number with respect to the microchannel width is observed for the silicon carbide porous medium, with values of 54.76% and 58.33% in the lower and upper directions, respectively.

Fig. 11 shows the variation of the Sherwood number against the change in thickness of the lower and upper walls for 90% porosity. At 90% porosity, unlike the 95% porosity case, the Sherwood number decreases with increasing channel height thickness for all cases (alumina, titanium dioxide, and silicon carbide). This indicates that reduced porosity leads to a decrease in convective mass transfer because there is less space for fluid flow and interaction with the porous environment. Here again, the Sherwood number for alumina is the lowest among the three porous environments, followed by titanium dioxide, and finally, silicon carbide has the highest value.

Interestingly, with comparison between fig. (10) and fig.

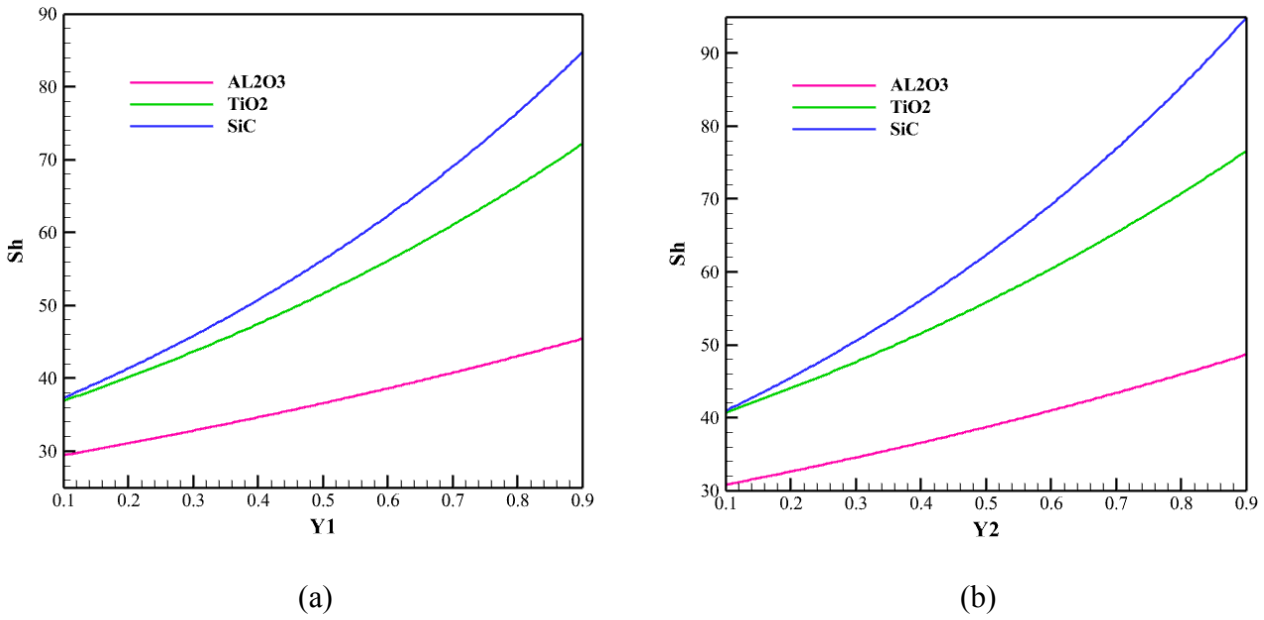

Fig. 10. The variation of the Sherwood number against the change in thickness: a) Lower wall and b) Upper wall with 95% porosity.

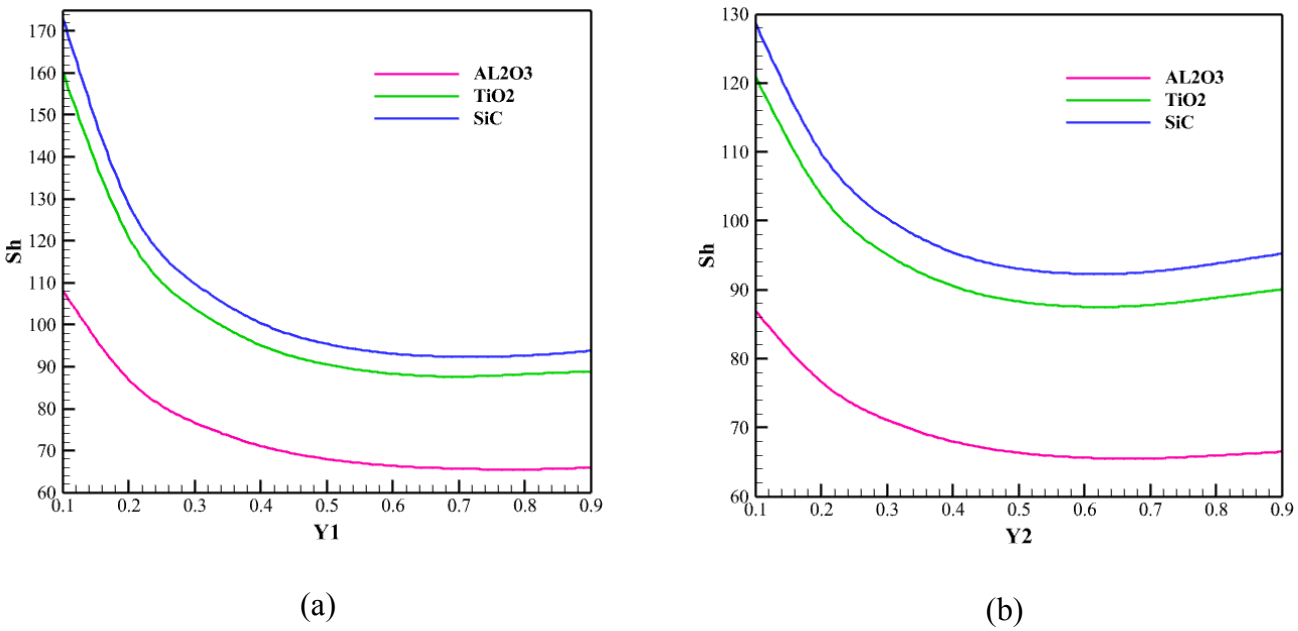

Fig. 11. The variation of the Sherwood number against the change in thickness: a) Lower wall and b) Upper wall with 90% porosity.

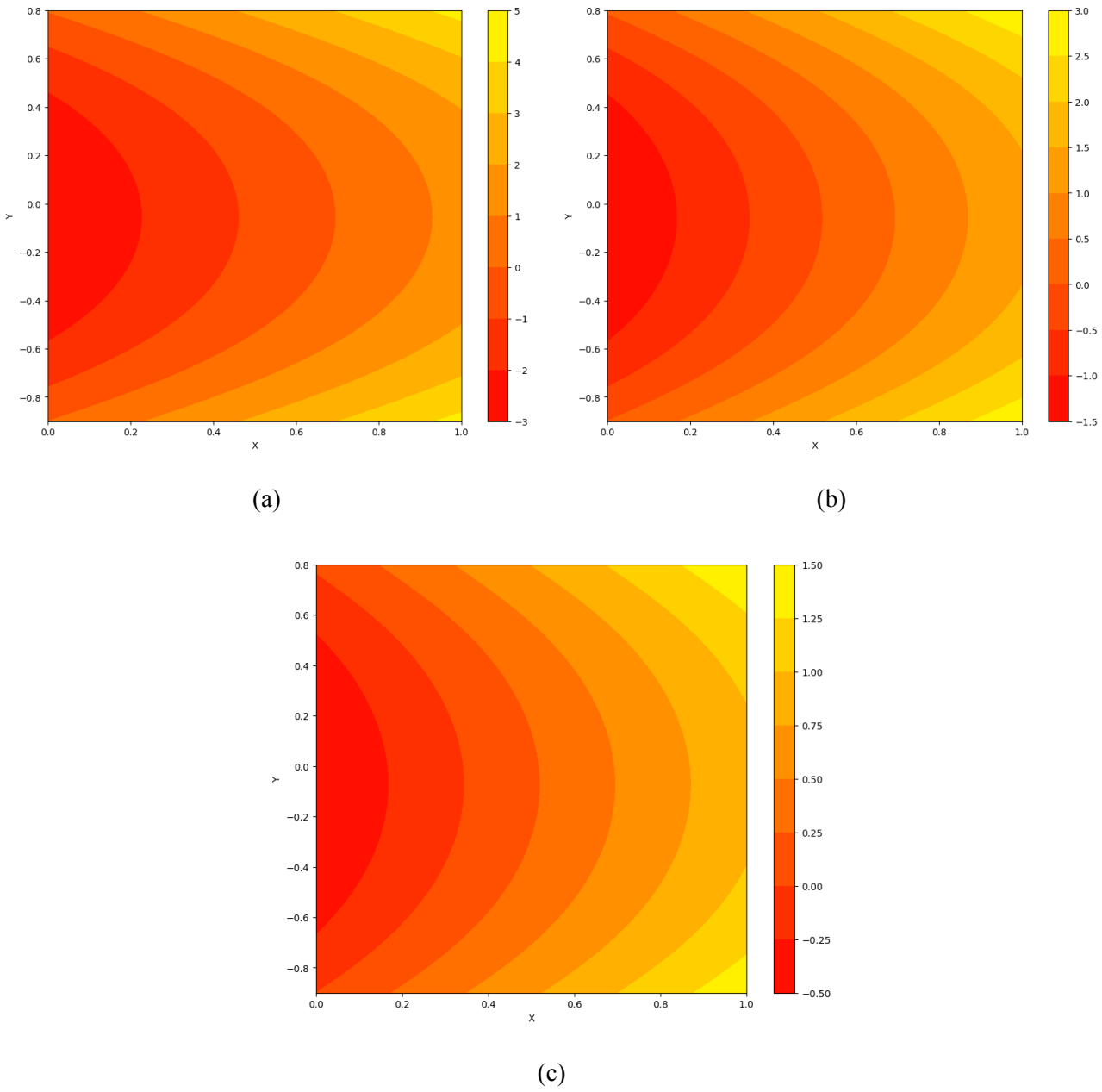

Fig. 12. The effect of porosity changes on the dimensionless temperature contour of the fluid phase for the porous medium of Al_2O_3 with porosities: a) 85%, b) 90% and c) 95%.

(11), the Sherwood number at 90% porosity decreases with increasing channel height thickness, contrary to the behavior observed at 95% porosity. This indicates that reduced porosity significantly impacts mass transfer. Another noteworthy point from Fig. 11(a) and (b) is that from a thickness of 0.1 to 0.4, the Sherwood number decreases steeply. This indicates that at lower heights, reduced porosity has a greater impact on mass transfer. Additionally, beyond a height thickness of 0.4, the Sherwood number remains almost constant, and its slope of decrease is low. This shows that at greater heights, the impact of reduced porosity on mass transfer is less significant.

Fig. 12 shows the effect of porosity change on the normalized temperature contour of the fluid phase for the porous medium of Al_2O_3 with porosities of 85%, 90%, and 95%. In Fig. 12(a), the fluid flows in the environment with the lowest porosity, and we observe the most significant temperature variations. The dimensionless temperature of the fluid phase fluctuates from -3 to 5, indicating a severe and almost harsh temperature gradient. These extensive changes transfer thermal energy at high speed and intensity. This condition clearly shows that reduced porosity causes severe in-homogeneities at temperature distribution, as if the fluid

is trying to adapt to more solid obstacles and experiences extreme temperatures in this process. For Fig. 12(b), with an increase in porosity to 90%, the temperature variations become slightly calmer. In this case, the dimensionless temperature of the fluid phase fluctuates between -1.5 to 3. Here, the temperature gradient is still significant but less intense. In this state, the fluid is relatively calmer but still has turbulent flows, although not as much as before. The increase in porosity allows the fluid to distribute thermal energy more efficiently, but significant in-homogeneities in the dimensionless temperature distribution still exist. This state represents a midpoint between chaos and order. Fig. 12(c), In this state, where we have the highest porosity, the fluid flows in a very open environment, and we observe the least temperature variations. The dimensionless temperature of the fluid phase varies from -0.5 to 1.5, indicating the lowest temperature gradient among the three states. Here, the fluid transfers thermal energy uniformly and harmoniously. The increase in porosity allows the fluid to encounter minimal resistance, resulting in a more balanced temperature distribution. This state represents the peak harmony between the fluid and the porous environment, where heat transfer shows its most optimal form. As the porosity coefficients increase from 85% to 95% the variation rates of fluid phase temperature are decreased from 78% to 45%.

Fig. 13 shows the effect of porosity change on the normalized temperature contour of the solid phase for the porous environment of Al_2O_3 with porosities of 85%, 90%, and 95%. In Fig. 13(a), in the state with the lowest porosity, the solid phase experiences the most significant dimensionless temperature variations. The dimensionless temperature of the solid phase fluctuates from -0.6 to 4.8, indicating a very severe temperature gradient and significant inhomogeneity in temperature distribution. The contour slopes in this state are very steep, as if the solid phase is trying to cope with the limitations caused by its high density. The temperature changes rapidly and intensely. This severe inhomogeneity shows that in high-density environments, the solid phase cannot distribute thermal energy uniformly, resulting in sharply distinct cold and hot spots.

In Fig. 13(b), with an increase in porosity to 90%, the dimensionless temperature variations of the solid phase become slightly calmer. The dimensionless temperature fluctuates between -0.4 to 3.2. The temperature gradient is still significant, but its intensity has decreased compared to the 85% porosity state. The contour slopes are still steep, but not as much as before. In this state, temperature changes are still noticeable but have moved away from the previous chaotic state. This state shows that an increase in porosity allows the solid phase to distribute thermal energy more efficiently, but significant in-homogeneities in temperature distribution still exist. In Fig. 13(c), in the state with the highest porosity (95%), the solid phase experiences the least dimensionless temperature variations. The dimensionless temperature of the solid phase fluctuates from -0.25 to 1.5, indicating the lowest temperature gradient among the three states. The contour slopes in this state are much gentler, as if the solid phase, in an open and calm environment, distributes thermal energy uniformly and harmoniously. In this state, temperature changes occur smoothly and in an orderly manner. The increase in porosity allows the solid phase to encounter minimal resistance, resulting in a more balanced temperature distribution. This state represents the peak harmony between the solid phase and the porous environment, where heat transfer shows its most optimal form. As the porosity coefficients increase from 85% to 95% the variation rates of fluid phase temperature are decreased from 65% to 35%.

Fig. 14 shows the effect of changing porosity on the hydrogen concentration contour for a porous alumina medium with porosity percentages of 85%, 90%, and 95%. In Fig. 14(a), where we have the lowest porosity (85%), hydrogen consumption is at its minimum. Hydrogen is primarily consumed on the walls, where the platinum catalyst is present, but almost no consumption is observed in the center of the channel. The hydrogen concentration in the center of the channel remains almost constant from start to end, as if the hydrogen in this region has been forgotten. The reason for this phenomenon can be attributed to the high density of the porous medium, which prevents the penetration and diffusion of hydrogen toward the walls. As a result, the surface reaction occurs only near the walls, and a significant portion of the hydrogen exits the channel unreacted. Fig. 14(b), With an increase in porosity to 90%, hydrogen consumption improves, but the highest consumption remains concentrated on the walls. In the center of the channel, hydrogen consumption has increased compared to the previous case, but it is still significantly lower than on the walls. The increase in porosity allows hydrogen to penetrate more effectively toward the walls, but there are still limitations that prevent complete hydrogen consumption in the center of the channel. This relative improvement indicates the positive effect of increased porosity on enhancing hydrogen access to the catalyst. Fig. 14(c) In this case, where the porosity is highest (95%), the maximum hydrogen consumption is observed. On the walls, hydrogen is completely consumed, and even in the center of the channel, approximately 50% of the hydrogen is nearly consumed. The increased porosity allows hydrogen to easily penetrate toward the walls and come into contact with the platinum catalyst. As a result, the surface reaction occurs more efficiently, and a significant portion of the hydrogen is consumed even in the center of the channel. This case represents the peak of harmony between the structure of the porous medium and the chemical reaction, where mass transfer and surface reactions are optimized to their fullest extent. With increasing the porosity coefficient, the rate of hydrogen to water conversion is increased from 43.01 to 75.05%.

Fig. 15 shows the effect of changing the position of the lower wall on the hydrogen concentration distribution at three positions: Y_1 = -0.1, -0.5, and -0.9. In case (a), where the channel height is the smallest (0.9), hydrogen begins to be consumed rapidly on the walls, and the hydrogen concentration on the walls reaches almost zero at approximately 0.001 of

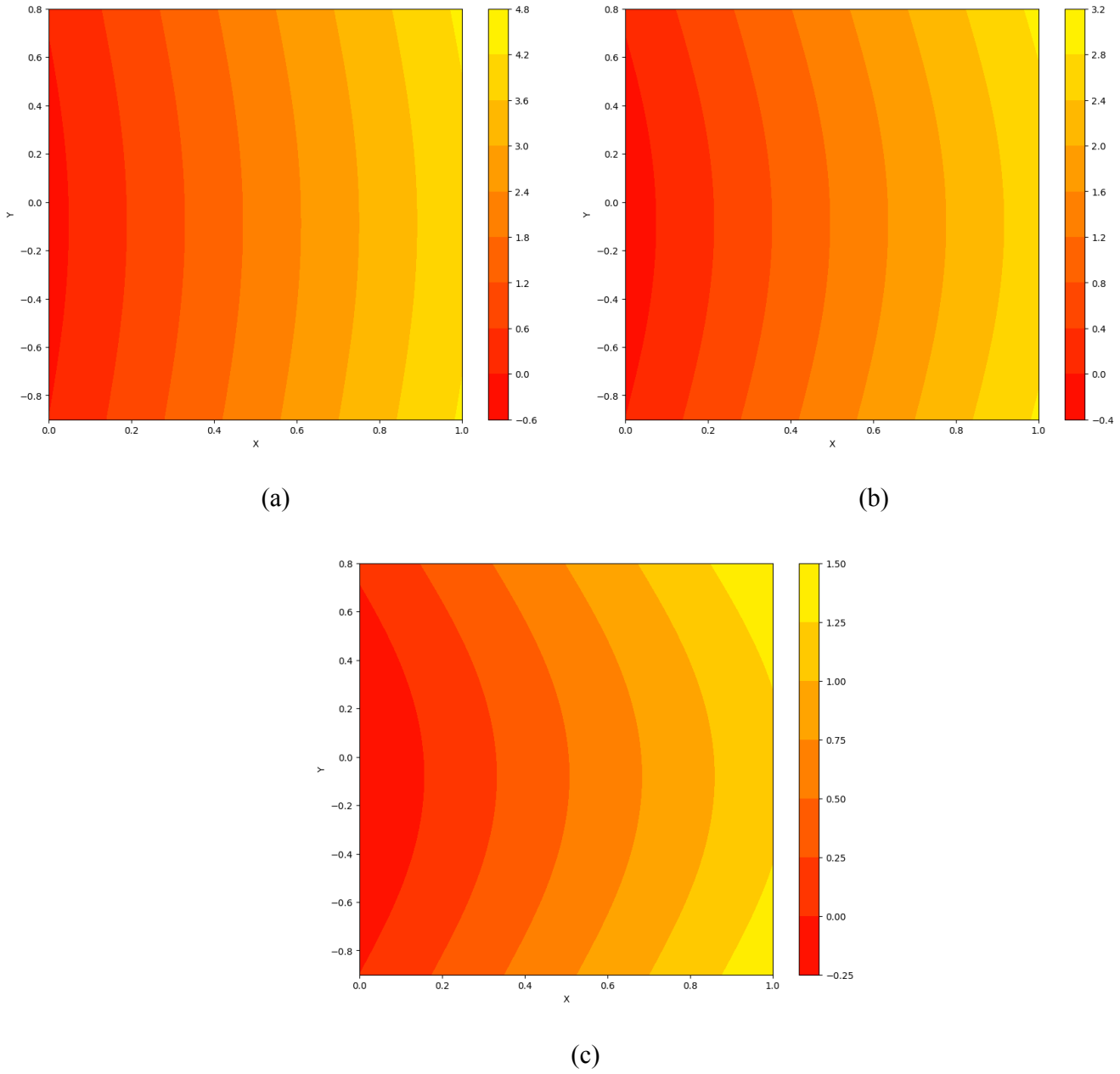

Fig. 13. The effect of porosity changes on the dimensionless temperature contour of the solid phase for the porous medium of Al_2O_3 with porosities: a) 85%, b) 90% and c) 95%.

the channel length. However, there is also a small amount of unconsumed hydrogen in the center of the channel. This scenario is akin to a shallow river where the flow quickly encounters obstacles and releases all its energy over a short distance. The reduction in channel height allows hydrogen to easily penetrate the walls and come into contact with the platinum catalyst. As a result, the surface reaction occurs quickly and with high efficiency. This case demonstrates that in channels with lower heights, mass transfer and chemical reactions are optimized more effectively. Fig. 15(b), With an increase in channel height to 1.3, hydrogen consumption remains rapid but not as much as in the previous case. Here, the hydrogen concentration on the walls also reaches nearly zero at approximately 0.001 of the channel length, but more hydrogen is consumed in the center of the channel compared to the first case. The increase in channel height causes hydrogen to reach the walls slightly later, but at the same time, it provides more opportunity for hydrogen to penetrate the center of the channel and react with the catalyst. This case represents a relative balance between the reaction rate and hydrogen consumption in the center of the channel. In Fig. 15(c), where the channel height is the largest (1.7), hydrogen consumption occurs later. The hydrogen concentration on the walls reaches zero for the first time at

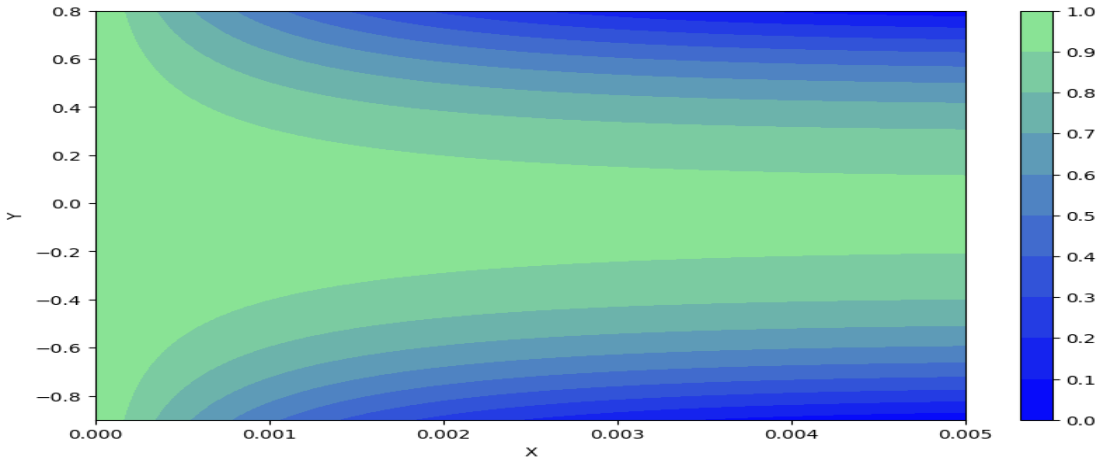

(a)

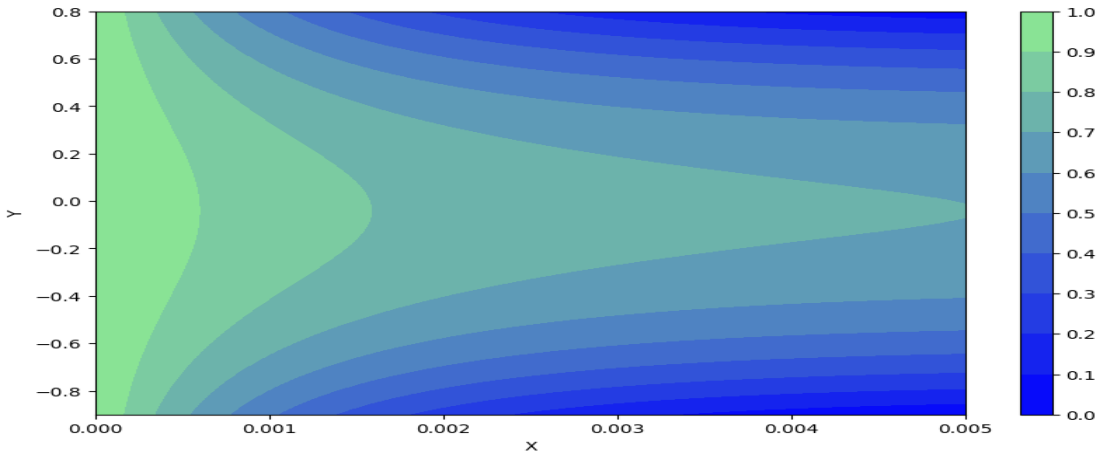

(b)

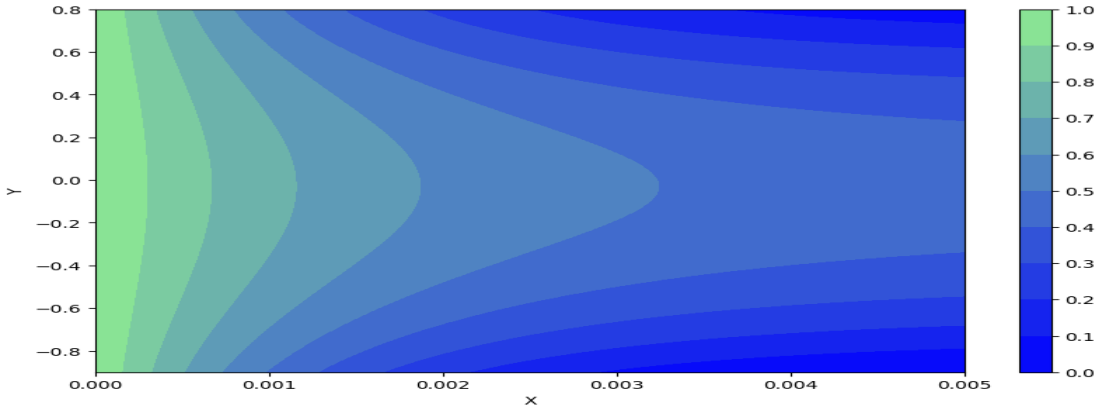

(c)

Fig. 14. The effect of changing porosity on the hydrogen concentration contour for Al_2O_3 with porosity percentages of a) 85%, b) 90%, and c) 95%.

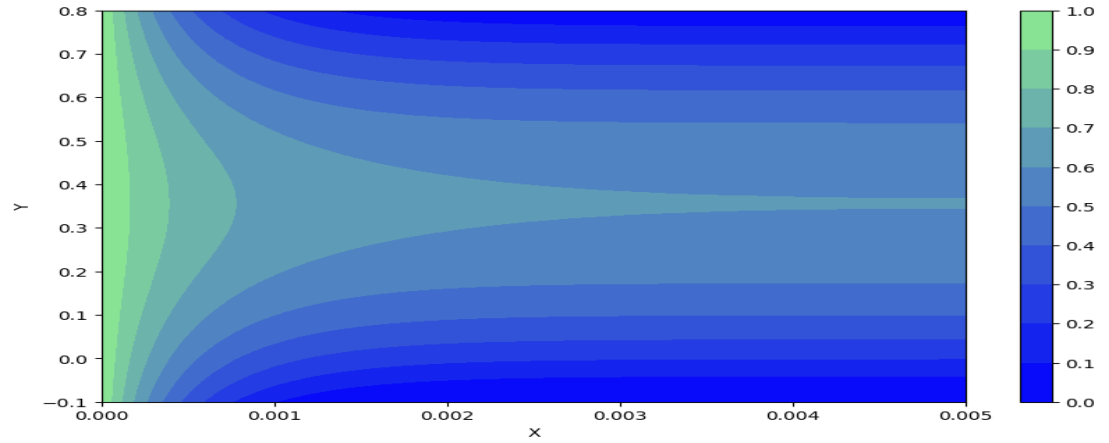

(a)

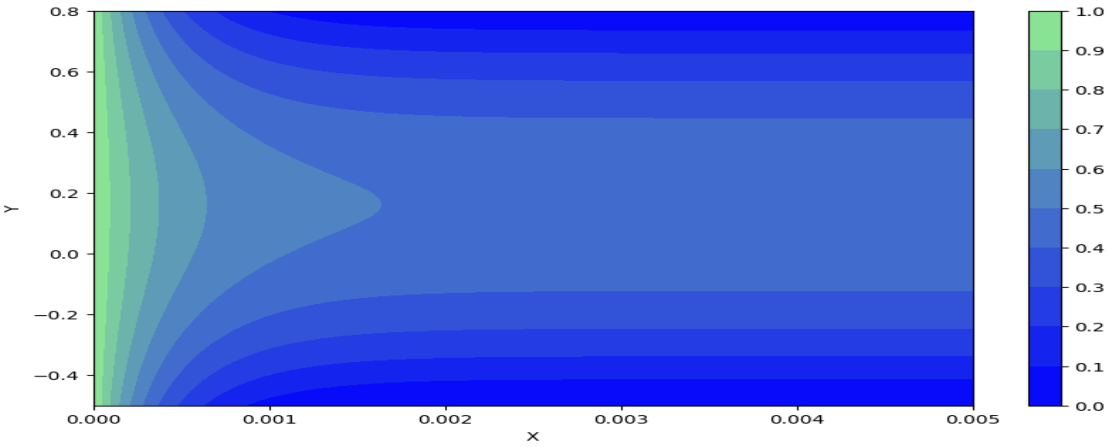

(b)

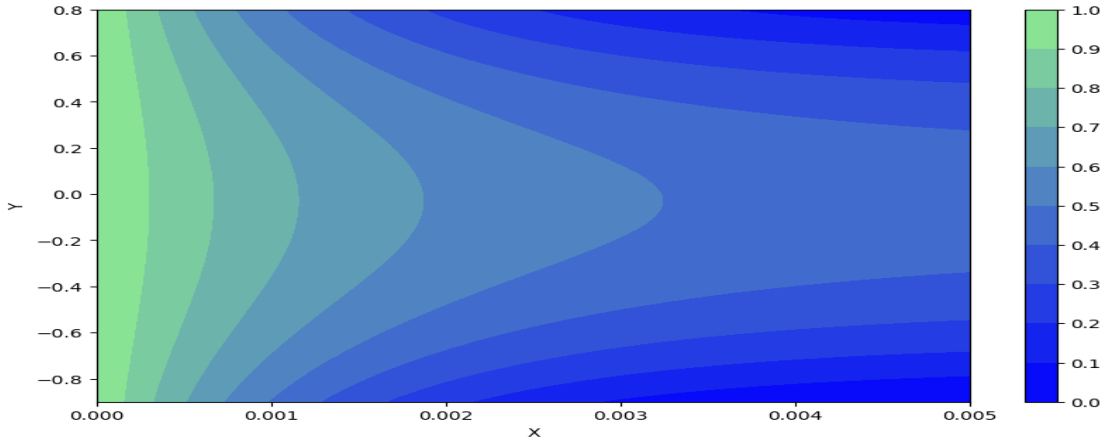

(c)

Fig. 15. The effect of changing the position of the lower wall on the hydrogen concentration distribution: a) Y_1 =-0.1, b) Y_1= -0.5, and c) Y_1= -0.9.

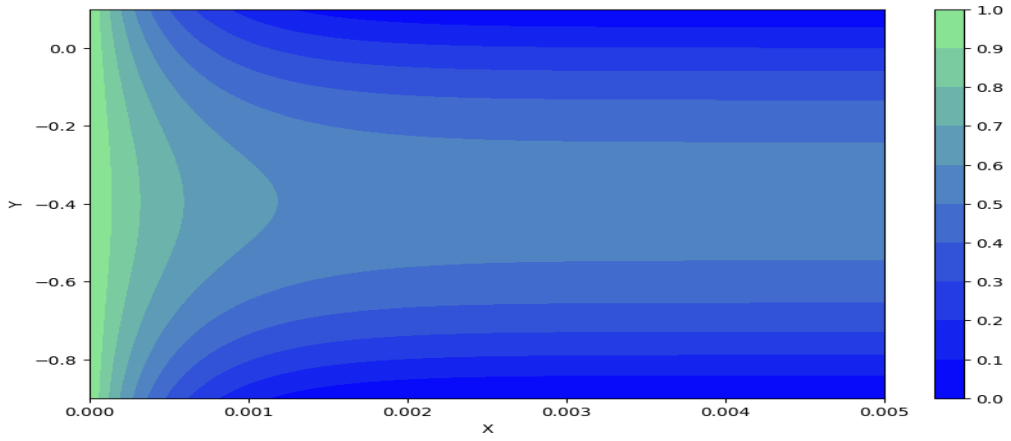

(a)

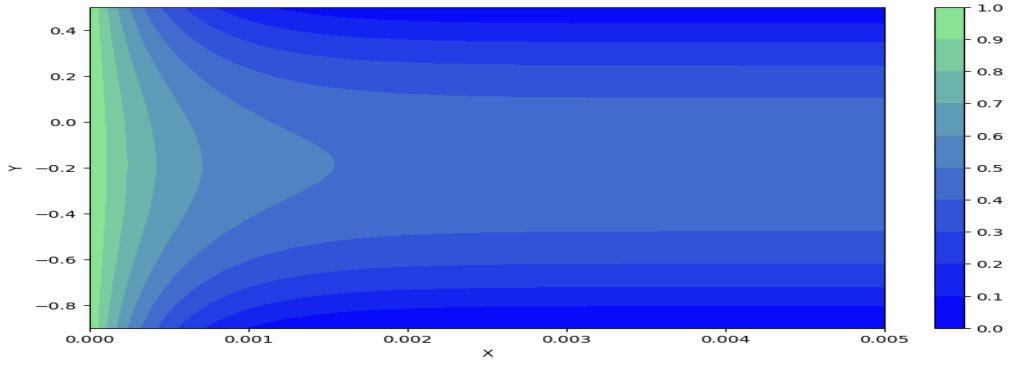

(b)

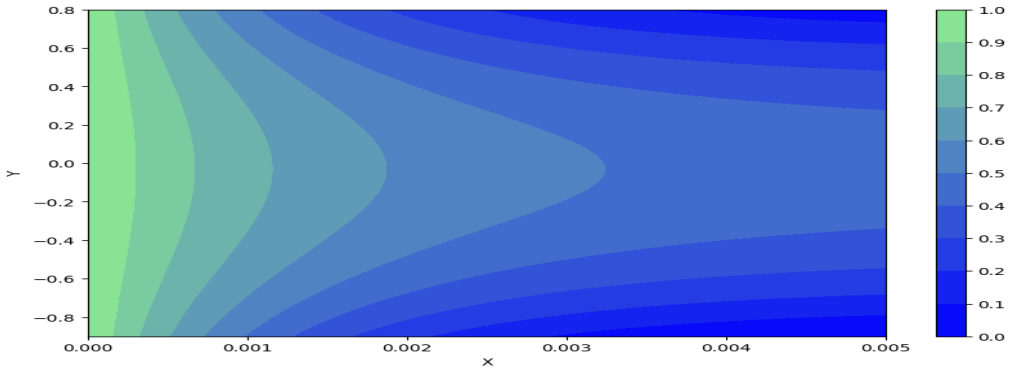

(c)

Fig. 16. The effect of changing the position of the upper wall on the hydrogen concentration distribution: a) Y_2 =-0.1, b) Y_2 = -0.5, and c) Y_2 = -0.8.

0.003 of the channel length, indicating a delay in the start of the reaction. However, the amount of hydrogen entering the channel in this case is greater than in the previous two cases, and hydrogen consumption in the center of the channel has also increased significantly. This case demonstrates that in channels with greater heights, although the reaction rate decreases, hydrogen consumption occurs more extensively and across a larger area of the channel. With increasing the lower wall thickness from 0.1 to 0.9, the rate of hydrogen to water conversion is increased from 30.01 to 47.05%.

Fig. 16 shows the effect of changing the position of the upper wall on the hydrogen concentration distribution at three

positions Y_1 = 0.1, 0.5 and 0.8. Fig. 16(a), In this case, where the channel height is the smallest, hydrogen begins to be consumed rapidly on the walls. Beyond 0.001 of the channel length, the hydrogen concentration on the walls nearly reaches zero, and even in the center of the channel, there is a small amount of unconsumed hydrogen. This scenario is akin to a shallow river where the flow quickly encounters obstacles and releases all its energy over a short distance. The reduction in channel height allows hydrogen to easily penetrate the walls and come into contact with the platinum catalyst. As a result, the surface reaction occurs quickly and with high efficiency. This case demonstrates that in channels with lower heights, mass transfer and chemical reactions are optimized more effectively. Fig. 16(b), With an increase in channel height to 1.4, hydrogen consumption remains rapid but not as much as in the previous case. Here, the hydrogen concentration on the walls also reaches nearly zero at approximately 0.001 of the channel length, but more hydrogen is consumed in the center of the channel compared to the first case. This scenario is similar to a moderately deep river where the flow is slightly slower but still releases its energy effectively. The increase in channel height causes hydrogen to reach the walls slightly later, but at the same time, it provides more opportunity for hydrogen to penetrate the center of the channel and react with the catalyst. This case represents a relative balance between the reaction rate and hydrogen consumption in the center of the channel. Fig. 16(c) In this case, where the channel height is the largest (1.7), hydrogen consumption occurs later. The hydrogen concentration on the walls reaches zero for the first time at 0.003 of the channel length, indicating a delay in the start of the reaction. However, the amount of hydrogen entering the channel in this case is greater than in the previous two cases, and hydrogen consumption in the center of the channel has also increased significantly. With increasing the upper wall thickness from 0.1 to 0.8, the rate of hydrogen to water conversion is increased from 25.52 to 39.12%.

6- Conclusion

In this work, the analytical model of low-temperature hydrogen/oxygen reactor with platinum surface reaction and three different porous mediums is presented. In this model, the non-asymptotic solution for governing equations of momentum, energy and mass concentration has been investigated. The main results of this work can be abbreviated as follows:

- Among the three micro-porous media under investigation, silicon carbide and alumina demonstrate the lowest and highest average normalized fluid temperatures, registering values of 0.15 and 0.50, respectively.
- Similarly, silicon carbide and alumina exhibit the lowest and highest average normalized solid-phase temperatures, with values of 0.15 and 0.60, respectively.
- The greatest span-wise variation in the Nusselt number within the microchannel is observed for the alumina porous medium, attaining 58.70% at 95% porosity and 67.69% at 90% porosity.
- The rate of hydrogen-to-water conversion in the alumina medium proceeds approximately 41% more rapidly than in titanium oxide and 67% more rapidly than in silicon carbide.
- The maximum span-wise variation in the Sherwood number across the microchannel occurs in the silicon carbide porous medium, reaching 58.33% at 95% porosity and 50.13% at 90% porosity.
- As porosity increases from 85% to 95%, the variation in fluid- and solid-phase temperatures diminishes from 78.01% to 45.09% and from 65.92% to 35.09%, respectively.
- Higher porosity facilitates deeper hydrogen penetration toward the channel walls, enhancing contact with the platinum catalyst and resulting in substantial hydrogen consumption even at the channel centerline.
- Increasing the porosity from 85% to 95% elevates the hydrogen-to-water conversion rate from 43.01% to 75.05%.
- Augmenting the lower wall thickness from 0.1 to 0.9 units raises the hydrogen-to-water conversion rate from 30.01% to 47.05%.
- Similarly, increasing the upper wall thickness from 0.1 to 0.8 units enhances the conversion rate from 25.52% to 39.12%.
- Practitioners may employ this novel analytical framework to construct precise models of electrolysis and hydrogen decomposition phenomena.
- Further development of this study could yield a comprehensive multi-reaction model suitable for industrial-scale hydrogen production.
- The present model is extensible to parametric formulations that integrate hydrogen generation with polymer electrolyte membrane fuel cells.

References

[1] B. Hellsing, B. Kasemo, V. Zhdanov, Kinetics of the hydrogen-oxygen reaction on platinum, Journal of Catalysis, 132(1) (1991) 210-228.

[2] P.-A. Bui, D. Vlachos, P. Westmoreland, Modeling ignition of catalytic reactors with detailed surface kinetics and transport: Oxidation of H2/air mixtures over platinum surfaces, Industrial & engineering chemistry research, 36(7) (1997) 2558-2567.

[3] H. Enomoto, H. Kato, M. Tsue, M. Kono, An numerical simulation of effect of surface diffusion on hydrogen-oxygen reaction over platinum catalytic surface, JSME International Journal Series B Fluids and Thermal Engineering, 42(1) (1999) 71-77.

[4] T.W. Tong, M.M. Abou-Ellail, Y. Li, Mathematical modeling of impinging hydrogen-air flows augmented by catalytic surface reactions, Journal of thermophysics and heat transfer, 22(4) (2008) 709-717.

[5] M. Abou-Ellail, T. Tong, Y. Li, Numerical simulation of hydrogen–air boundary layer flows augmented by catalytic surface reactions, ASME Journal of Heat and Mass Transfer, 133(11) (2011).

[6] A. Fanaee, J. Esfahani, The investigation of semi-three-dimensional heat transfer modeling in microcombustors,

Journal of Thermal Science and Engineering Applications, 3(1) (2011).

[7] R.S. Amano, M.M. Abou-Ellail, S. Elhaw, M. Saeed Ibrahim, Numerical simulation of hydrogen–air reacting flows in rectangular channels with catalytic surface reactions, Heat and Mass Transfer, 49(9) (2013) 1243-1260.

[8] A. Ates, P. Pfeifer, O. Görke, Thin-Film Catalytic Coating of a Microreactor for Preferential CO Oxidation over Pt Catalysts, Chemie Ingenieur Technik, 85(5) (2013) 664-672.

[9] E. Lalik, R. Kosydar, R. Tokarz-Sobieraj, M. Witko, T. Szumełda, M. Kołodziej, W. Rojek, T. Machej, E. Bielańska, A. Drelinkiewicz, Humidity induced deactivation of Al2O3 and SiO2 supported Pd, Pt, Pd-Pt catalysts in H2+ O2 recombination reaction: The catalytic, microcalorimetric and DFT studies, Applied Catalysis A: General, 501 (2015) 27-40.

[10] V. Paunovic, J.C. Schouten, T. Nijhuis, Direct synthesis of hydrogen peroxide in a wall-coated microchannel reactor over Au–Pd catalyst: A performance study, Catalysis Today, 248 (2015) 160-168.

[11] J. Esfahani, S.A. Fanaee, Analytical modeling of hydrogen–air mixture in a catalytic microchannel, Journal of Thermophysics and Heat Transfer, 29(2) (2015) 274-280.

[12] R. Sui, N.I. Prasianakis, J. Mantzaras, N. Mallya, J. Theile, D. Lagrange, M. Friess, An experimental and numerical investigation of the combustion and heat transfer characteristics of hydrogen-fueled catalytic microreactors, Chemical Engineering Science, 141 (2016) 214-230.

[13] Q. Li, J. Wang, L. Meng, J. Li, Z. Guo, CFD study on stability limits of hydrogen/air premixed flames in planar micro-combustors with catalytic walls, Applied Thermal Engineering, 121 (2017) 325-335.

[14] W. Yu, J. Tao, X. Yu, S. Zhao, S.-T. Tu, H. Liu, A microreactor with superhydrophobic Pt–Al2O3 catalyst coating concerning oxidation of hydrogen off-gas from fuel cell, Applied Energy, 185 (2017) 1233-1244.

[15] F. Giarratano, G. Arzac, V. Godinho, D. Hufschmidt, M.J. De Haro, O. Montes, A. Fernández, Nanoporous Pt-based catalysts prepared by chemical dealloying of magnetron-sputtered Pt-Cu thin films for the catalytic combustion of hydrogen, Applied Catalysis B: Environmental, 235 (2018) 168-176.

[16] J. Pan, Y. Zhang, Q. Lu, X. Shao, E.K. Quaye, Y. Zhu, Numerical study on stability and influencing factors of heterogeneous reaction for hydrogen/oxygen mixture in planar catalytic micro combustor, International Journal of Hydrogen Energy, 44(29) (2019) 15587-15597.

[17] G. Hunt, N. Karimi, B. Yadollahi, M. Torabi, The effects of exothermic catalytic reactions upon combined transport of heat and mass in porous microreactors, International Journal of Heat and Mass Transfer, 134 (2019) 1227-1249.

[18] M. Bazdar, A. Irankhah, Water-gas shift reaction in a microchannel Ni-based catalytic coated reactor: effect of solvents, Chemical Engineering & Technology, 43(12) (2020) 2428-2436.

[19] R. Serra-Maia, J.D. Rimstidt, F.M. Michel, Kinetic effect of surface chemisorbed oxygen on platinum-catalyzed hydrogen peroxide decomposition, Catalysis Letters, 151(1) (2021) 138-146.

[20] G.R. Hunt, Analytical and numerical investigation of heat and mass transport in catalytic microreactors, University of Glasgow, 2020.

[21] A. Edalati nejad, S.A. Fanaee, M. Ghodrat, Numerical investigation of methane-air counterflow premixed flame into a newly designed plus-shaped chamber with platinum and rhodium catalysts coated walls, Combustion Science and Technology, 195(11) (2023) 2598-2613.

[22] H. Dai, S. Lv, Q. Cui, Z. Guo, Z. Jiang, Partial oxidation of methane in the catalytic porous media with the combination of hexaaluminate and spinel, International Journal of Hydrogen Energy, 87 (2024) 344-360.

[23] C. Di Paola, E. Plekhanov, M. Krompiec, C. Kumar, E. Marsili, F. Du, D. Weber, J.S. Krauser, E. Shishenina, D. Muñoz Ramo, Platinum-based catalysts for oxygen reduction reaction simulated with a quantum computer, NPJ Computational Materials, 10(1) (2024) 285.

[24] J.A. Esfahani, S.A. Fanaee, F. Ahmadi, M.A. Rad, The analytical model of flame characteristics of hydrogen–air through wall and gas interaction analysis, Heat Transfer, 54(1) (2025) 1014-1030.

[25] S. Fanaee, Self-similar nonasymptotic solution of multireaction stationary flow in catalytic microcombustor, Journal of Thermophysics and Heat Transfer, 32(3) (2018) 560-569.

[26] A. Etbaeitabari, M. Barakat, A. Imani, G. Domairry, P. Jalili, An analytical heat transfer assessment and modeling in a natural convection between two infinite vertical parallel flat plates, Journal of Molecular Liquids, 188 (2013) 252-257.

[27] P. Jalili, B. Jalili, A. Shateri, D.D. Ganji, A novel fractional analytical technique for the time-space fractional equations appearing in oil pollution, Int. J. Eng, 35(12) (2022) 2386-2394.

[28] P. Jalili, B. Jalili, I. Ahmad, A.S. Hendy, M.R. Ali, D.D. Ganji, Python approach for using homotopy perturbation method to investigate heat transfer problems, Case Studies in Thermal Engineering, 54 (2024) 104049.

[29] P. Majidi Zar, A. Shateri, P. Jalili, F.A. Al-Yarimi, B. Jalili, D.D. Ganji, N. Ben Khedher, Radiative effects on 2D unsteady MHD Al2O3-water nanofluid flow between squeezing plates: A comparative study using AGM and HPM in Python, ZAMM-Journal of Applied Mathematics and Mechanics/Zeitschrift für Angewandte Mathematik und Mechanik, 105(2) (2025) e202400546.

[30] B. Jalili, A.M. Ganji, A. Shateri, P. Jalili, D.D. Ganji, Thermal analysis of non-Newtonian visco-inelastic fluid MHD flow between rotating disks, Case Studies in Thermal Engineering, 49 (2023) 103333.

[31] S. Hajizadeh, B. Jalili, P. Jalili, D.D. Ganji, H. Ahmad, Influence of flow parameters in incompressible electrically conducting fluid over a stretching plate with a surface condition factor, ZAMM-Journal of Applied Mathematics and Mechanics/Zeitschrift für Angewandte

Mathematik und Mechanik, 105(5) (2025) e70075.

[32] A. Shateri, M.M. Moghaddam, B. Jalili, Y. Khan, P. Jalili, D.D. Ganji, Heat transfer analysis of unsteady nanofluid flow between moving parallel plates with magnetic field: analytical approach, Journal of Central South University, 30(7) (2023) 2313-2323.

[33] B. Jalili, M. Emad, P. Jalili, D.D. Ganji, S. Saleem, E.M. Tag-eldin, Thermal analysis of boundary layer nanofluid flow over the movable plate with internal heat generation, radiation, and viscous dissipation, Case Studies in Thermal Engineering, 49 (2023) 103203.

Nomenclature

a_{sf}	interfacial area per unit volume of porous media, (m^{-1})
Bi	Biot number
Br'	modified Brinkman number
C	mass species concentration $(kg.m^{-3})$
C_0	inlet concentration $(kg.m^{-3})$
C_p	specific heat capacity $(J.K^{-1}.kg^{-1})$
C_b	Balk concentration $(kg.m^{-3})$
C_M	molar density $(kg.m^{-3})$
D	mass diffusion coefficient $(m^2 s^{-1})$
Da	Darcy number
D_T	coefficient of thermal mass diffusion $(m.K^{-1}.kg^{-1}.s^{-1})$
h_1	half – thickness of the microchannel to lower wall (m)
h_2	half – thickness of the microchannel to upper wall (m)
h_3	half – height of microchannel (m)
h_{sf}	interstitial heat transfer coefficient $(W.K^{-1}.m^{-2})$
H_w	wall heat transfer coefficient $(W.K^{-1}.m^{-2})$
k	effective thermal conductivity ratio of the fluid and the porous solid
k_1	thermal conductivity of wall 1 $(W.K^{-1}.m^{-1})$
k_2	thermal conductivity of wall 2 $(W.K^{-1}.m^{-1})$
k_{e1}	ratio of thermal conductivity of wall 1 and thermal conductivity of the porous solid
k_{e2}	ratio of thermal conductivity of wall 2 and thermal conductivity of the porous solid
k_{ef}	effective thermal conductivity of the fluid phase $(W.K^{-1}.m^{-1})$
k_{es}	effective thermal conductivity of the solid phase of the porous medium $(W.K^{-1}.m^{-1})$
k_R	reaction rate constant on the walls $(m.s^{-1})$
L	length of the microchannel (m)
M	viscosity ratio
Nu	Nusselt number
p	Pressure (Pa)
Pe	Peclet number
Q	wall heat flux ratio
q_c''	total catalytic heat flux $(W.m^{-2})$
q_{w1}''	lower wall heat flux $(W.m^{-2})$
q_{w2}''	upper wall heat flux $(W.m^{-2})$
Re	Reynolds number
R	specific gas constant $(J.K^{-1}.kg^{-1})$
S	shape factor of the porous medium
Sr	Soret number
Sh	Sherwood number
T	Temperature (K)
u	fluid velocity $(m.s^{-1})$

$\overline{u}$	$average velocity over cross-section (m.s^{-1})$
x	*dimensional axial coordinate*
X	*dimensionless axial coordinate*
y	*dimensional transverse coordinate*
Y	*dimensionless transverse coordinate*

Greek symbols

μ	*dynamic viscosity*
κ	*permeability*
ρ	*density*
θ	*dimensionless temperature*
ϕ	*dimensionless concentration*
ξ	*aspect ratio of the microchannel*
ε	*porosity of the porous medium*
γ	*Damköhler number*
λ	*Eigenvalue*

Subscripts

f	*Fluid*
s	*Porous solid*
1	*Lower wall*
2	*Upper wall*

HOW TO CITE THIS ARTICLE
S. Sisban, S. Abouzar Fanaee, The Novel Analytical Model of Low-Temperature Hydrogen/ Oxygen Reactor on Platinum Catalytic Surface in Different Micro-Porous Mediums, AUT J. Mech Eng., 10(3) (2026) 269-296.

DOI: 10.22060/ajme.2025.24784.6229